SOLAR-SAIL INVARIANT OBJECTS IN THE SUN-EARTH SYSTEM AND TRANSFERS TO THE L_5 REGION

MASTER THESIS

Alvaro Fernandez Mora
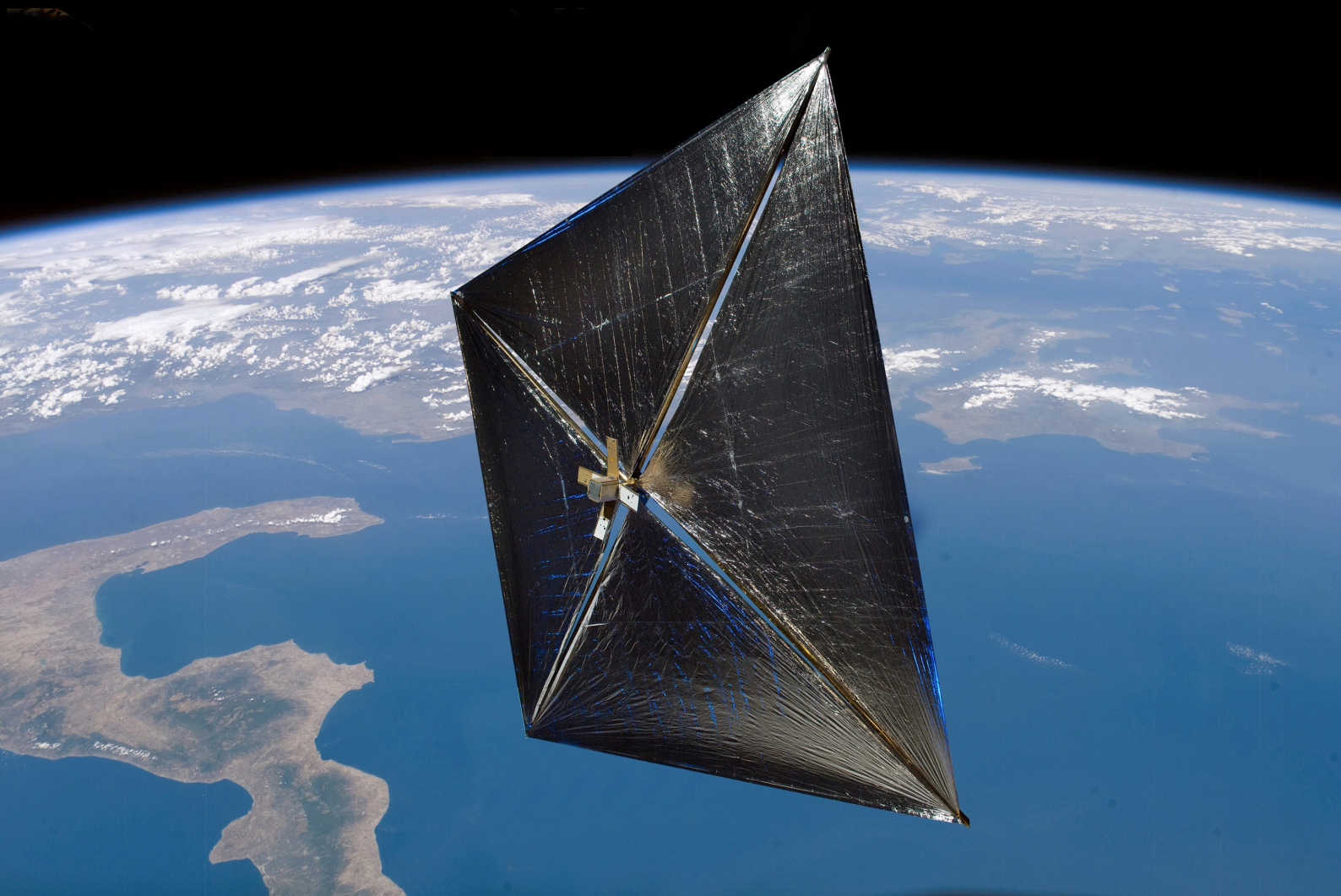
TUDelft

SOLAR-SAIL INVARIANT OBJECTS IN THE SUN-EARTH SYSTEM AND TRANSFERS TO THE L_5 REGION

MASTER THESIS

by

Alvaro Fernandez Mora

to obtain the degree of Master of Science in Aerospace Engineering,
at Delft University of Technology,
to be defended in public on Thursday 28 February 2019 at 1:45 p.m.

Supervisor:	Dr. M. J. Heiligers	
Thesis committee:	Prof. P. N. A. M. Visser	Committee chair
	Dr. M. J. Heiligers	Supervisor
	Dr.ir. W.T. van Horssen	External examinator

An electronic version of this dissertation is available at
http://repository.tudelft.nl/.

CONTENTS

LIST OF FIGURES

NOMENCLATURE

List of Symbols

α	Cone angle
δ	Clock angle
I	identity matrix
J_c	Jacobi constant
j_c	Normalised Jacobi constant
JG	Jacobian of G
α_0	Decision variable for genetic algorithm
α_f	Decision variable for genetic algorithm
α_i	Cone angle for segment i
$\bar{t}$	Orbit family tangent
$\bar{G}$	Constraint for the multiple shooting differential corrector
$\bar{t}_i$	Component i of the orbit family tangent
β	Lightness number
β^*	Lightness number for geometric changes in periodic orbits families
$\mathbf{x}$	Vector of decision variables for genetic algorithm
$\boldsymbol{\omega}$	Vector of frequencies of invariant tori
$\boldsymbol{\theta}$	Vector of angular variables of invariant tori
$\boldsymbol{\theta}_0$	Constant vector of angular variables of invariant tori
$\boldsymbol{a}$	Solar sail acceleration vector
$\boldsymbol{c}$	Generic point of invariant manifold
$\boldsymbol{c}$	Vector of Fourier coefficients
$\boldsymbol{c}_k$	Complex Fourier coefficient
$\boldsymbol{n}$	Sail normal vector
$\boldsymbol{p}$	Base vector of the local sail frame
$\boldsymbol{q}$	Base vector of the local sail frame
$\boldsymbol{r}_{eb}$	Earth-body vector

$\boldsymbol{r}_{sb}$	Sun-body vector
$\boldsymbol{u}$	Vector of the discretised invariant curve
$\boldsymbol{u}_s$	Stable eigenvector of equilibrium point
$\boldsymbol{u}_u$	Unstable eigenvector of equilibrium point
$\boldsymbol{v}$	Generic point of invariant manifold
$\boldsymbol{x}$	Phase space point
$\boldsymbol{X}$	Extended vector for the multiple shooting differential corrector
$\boldsymbol{x}_0$	Departure point of primary mission trajectory
$\boldsymbol{x}_e$	Equilibrium point
$\boldsymbol{X}_i$	Decision vector for the multiple shooting differential corrector for $i \in \{1, 2, ..., n\}$
$\boldsymbol{x}_i$	Node for segment i
$\boldsymbol{x}_p$	Periodic orbit point
$\boldsymbol{x}_{fixed}$	Fixed point
$\boldsymbol{y}$	Eigenvector of periodic orbit
$\boldsymbol{Y}$	(Un)stable eigenvector of quasi-periodic orbit
$\boldsymbol{y}_s$	Stable eigenvector of periodic orbit
$\boldsymbol{y}_u$	Unstable eigenvector of periodic orbit
$\boldsymbol{z}$	Generic point of periodic orbit
$\delta\rho_i$	Rotation for the multiple shooting differential corrector for $i \in \{0, f\}$
δS	Continuation step
δT	Update for periodic orbit period
ΔV	Velocity increment
δx_i	Update for component i of periodic orbit point
δX	Updte for X
δx	Update for periodic orbit point
δ_0	Decision variable for genetic algorithm
δ_f	Decision variable for genetic algorithm
δ_i	Clock angle for segment i

F_i First integral

G Map for periodic orbits computation

g_f Constraint on last node

g_i Constraint for $i = 0, f$

H Hamiltonian

h Generic functional

h_i Generic function with $i \in \{1, 2\}$

J Sympectic matrix

$J\bar{G}$ Jacobian of $\bar{G}$

$J\mathring{G}$ Jacobian of G

$J\tilde{G}$ Jacobian of $\tilde{G}$

Jg_i Jacobian of g_i for $i = 0, f$

JS Jacobian of S

K Index set

L_i Lagrange point for $i \in \{1, 2, ...5\}$

M Monodromy matrix

M_f Generic manifold

Q Fourier coefficient rotation operator

R Rotation operator

r_p Projection of the Sun-body vector onto the xy plane

S System of the multiple shooting differential corrector

s_i Stability index for $i \in \{1, 2\}$

SL_i Displaced Lagrange points for $i \in \{1, 2, ..., 5\}$

T Periodic orbit period

t time

T^* Period of periodic orbit solution

T_0 Time of flight for transfer

T_1 Period of departure periodic orbit

T_2 Period associated with ω_2

t_i Duration of segment i

T_n Period of arrival periodic orbit

T_p Duration of primary mission transfer

T_{2i} Period associated with ω_2 for $i = 0, f$

u Matrix for the multiple shooting differential corrector

u_i Real part of eigenvalue for $i \in \{1, 2, 3\}$

v_i Imaginary part of eigenvalue for $i \in \{1, 2, 3\}$

W^c Centre manifold

W^s Stable manifold

W^u Unstable manifold

x_i Component i of $\boldsymbol{x}$

y_{max} Maximum y value

z_{max} Maximum z value

Abbreviations

CIR Corotation interaction region

CME Coronal mass ejection

CR3BP Circular restricted three-body problem

DFT Discrete Fourier Transform

HO Halo orbit

JAXA Japan Aerospace Exploration Agency

KAM Kolmogórov-Arnold-Moser

NASA National Aeronautics and Space Administration

PLO Planar Lyapunov orbit

QPO Quasi-periodic orbit

SRP Solar radiation pressure

STM State transition matrix

TOF Time of flight

SUMMARY

The purpose of the research conducted for this thesis is to contribute to the understanding of solar-sail bounded motion in the Sun-Earth circular restricted three-body problem with solar radiation pressure and determine what transfers are possible between invariant objects in the vicinity of Earth and the L_5 region.

The Sun-Earth region around the L_4 and L_5 points is of particular interest for space missions related to space weather and search for Trojan asteroids. The equilateral Lagrange points are stationary points located 60 degrees ahead and behind Earth. Therefore, they grant observational access to regions of the Sun that are inaccessible from the L_1 point; which has been the destination of all space weather missions to date. A spacecraft in the vicinity of the L_5 point could provide earlier predictions of geomagnetic storms and coronal mass ejections. Furthermore, corotation interaction regions can also be studied from the L_5 vicinity. Regarding the search for Trojan asteroids, it is known that there exist stable regions around the equilateral libration points and asteroids have been found in orbit around these points in several systems. A mission to the L_5 point could therefore detect asteroids that so far have not been discovered. The scientific interest in the L_5 region is therefore current and broad.

In this thesis, the methodology for the computation of equilibrium points, periodic orbits, quasi-periodic orbits and invariant manifolds is applied to compute natural and solar-sail invariant objects for a range of sail performances expressed through the lightness number. The properties of the invariant objects in terms of existence, shape and stability are also studied as a function of the lightness number. Subsequently, solar-sail transfers between different invariant objects in the vicinity of Earth and the L_5 region are computed and optimised. First, initial guesses are found with a multi-objective genetic algorithm that obtains near-feasible transfers. A vector of decision variables defines these initial guesses that leverage the unstable manifolds from the departure invariant objects in the vicinity of Earth and backwards flow from the arrival ones in the L_5 region. Such near-feasible guesses then converge to fully feasible trajectories through a multiple shooting differential corrector. Finally, with a continuation strategy, the time of flight for the transfers is optimised resulting in near time-optimal transfers.

The main conclusions of the work can be summarised as follows. The surfaces of equilibria vary with the lightness number and after some threshold isolated surfaces merge. While certain families of periodic orbits present a change in their geometric behaviour with the lightness number, the evolution of their stability maintains the same trends. Solar-sail families of quasi-periodic orbits exist around periodic orbits with a central part. Furthermore, the families of Lissajous orbits around vertical and planar Lyapunov orbits around the collinear equilibrium points in the vicinity of Earth are connected for a range of Jacobi constants. Lastly, two types of quasi-periodic orbits were observed around the planar Lyapunov orbits in the L_5 region while only one type was found around the vertical Lyapunov orbits.

The transfers considered depart from the collinear equilibrium points in the vicinity of Earth, families of periodic and quasi-periodic orbits around those equilibrium points as well as from the invariant manifolds of the periodic orbits. For the arrival conditions, families of periodic and quasi-periodic orbits in the L_5 region were considered. The genetic algorithm in combination with the differential corrector and continuation produce fast solar-sail transfers ranging from 391 to 1194 days, depending on the case. In general, the type of invariant object does not have a significant effect on the time of flight of the transfers, but the equilibrium points the invariant objects are associated to do.

This thesis has provided a deeper insight into the types of solar-sail bounded motion in the Sun-Earth system and has successfully developed and applied a novel methodology to compute transfers between invariant objects that can be used for the preliminary trajectory design of a mission to the L_5 region.

PREFACE

I have always found what is absolute to be of particular beauty; that which cannot be refuted or denied because it is simply true (whatever that means). Therefore, I started to look for a master thesis topic that dealt with the fundamental aspects of celestial mechanics in its natural language: mathematics. Such search lead me to Jeannette Heiligers and solar sails. I quickly realised of the depth of the field and how much of an abstraction it was possible to make from what flies in the sky. In spite of finding it intimidating, I felt excited about comprehending the rigorous description of the motion of bodies in space. Such excitement took me sometimes away from the role of an engineer, but the more insight I gained the more ideas I could consider.

Jeannette and I came up with a project that combined theoretical ideas on bounded motion with applications to mission design. In fact, part of this thesis was conducted at NASA Marshall Space Flight Center for a mission proposal. Applying your own work to a potentially actual mission was certainly a very motivating experience. Furthermore, part of the thesis was presented as a conference paper at the 7th International Conference on Astrodynamics Tools and Techniques (ICATT). I was glad to be approached by some considering similar problems and interested in the work.

This journey through the aerospace engineering studies would certainly not have been possible without those who stood by my side. I would like to first thank my parents for their unconditional support. I would also like to thank my sisters for caring in the distance. To my friends in Seville, I thank your always curious questions about space stuff. Also, I thank the wolbodoers for making Delft an interesting place to live in. Lastly, I would like to thank Jeannette for her dedication and valuable input throughout the thesis. Without a doubt, this thesis would not be what it is if it had not been for your help.

Alvaro Fernandez Mora
Delft, February 2019

1

INTRODUCTION

1.1. SOLAR SAILING HISTORY

In 1862, radiation pressure was theoretically predicted by James Clerk Maxwell and was experimentally measured by Peter Levendew in 1900. These results led to the first consideration of solar radiation pressure (SRP) as the propelling mechanism for spacecraft in the 1920s from the minds of Konstantin Tsiolkovsky and Fridrickh Tsander. They worked on the idea of spacecraft propelled by light using large mirrors [2]. From this point on, solar sailing grew to transcend from the theoretical into the real world. It was not until May 2010 that the first solar-sail mission successfully measured the acceleration induced by SRP and performed attitude control with SRP. JAXA's Interplanetary Kite-craft Accelerated by Radiation Of the Sun (IKAROS), deployed a 14 x 14 m^2 square solar sail by centrifugal force. The mission was a technology demonstration for solar-sail technology as well as for the thin solar cells equipped on the reflecting film. Furthermore, it aimed at analyzing the solar radiation force attained [3]. Shortly after, NanoSail-D2 from NASA's Marshall Space flight Center and Ames Research Center was launched: a three units CubeSat inside the FASTSAT satellite to test the deployment mechanism of a 10 m^2 sail. The CubeSat initially failed to separate from FASTSAT, but on January 2011 it was ejected and successfully deployed its sail. Its twin brother, NanoSail-D, was designed for the same purpose and was previously launched in 2008 on a Falcon 1, but the satellite was lost due to a problem with the launcher [4]. The Planetary Society, following their enthusiasm for solar sails, started a new project in 2009: LightSail, consisting of another three units CubeSat with two units dedicated to a 5.5 x 5.5 m^2 sail. In 2015, the spacecraft was launched into a slightly lower orbit than desired, but the deployment was successful. Because of the atmospheric drag in the low-altitude Earth orbit, the satellite shortly re-entered and burned up in the atmosphere [5]. Future solar-sail missions include, for 2019, The Planetary Society's follow-up of LightSail, LightSail 2, and NASA's NEA Scout mission. NEA Scout will use a six units CubeSat with a nearly 83 m^2 sail to explore Near Earth Asteroids [6].

1.2. MISSION TO THE L_5 REGION

The Sun-Earth L_1 point is an ideal location for solar observation and to monitor space weather and Sun-Earth interactions. SOHO, ACE and WIND, among others, are in orbit around this point. Furthermore, the Sun-Earth L_2 point offers a cold and stable environment making it ideal for astrophysics research and deep space observation. For this reason it has been and it will be home to missions like Plank in the past, Gaia today and the James Webb Space Telescope in the future. The Earth-Moon Lagrange points are also of interest. A communication satellite at the L_2 point would make it possible to keep contact with a future base on the far side of the Moon.

The Sun-Earth equilateral libration points are very suitable to study space weather. Since they are stationary 60 degrees ahead and behind Earth, they can observe regions of the Sun inaccessible from Earth or the L_1 point. The satellite ACE at the L_1 point allows detecting geomagnetic storms about an hour before they hit Earth, but spacecraft in orbit around the equilateral points would allow a significant increase in this warning time [7]. Both equilateral points are suitable to study coronal mass ejections (CME); however, only the L_5 point is useful for studying corotation interaction regions (CIR), as they pass by the L_5 point first, then Earth and then the L_4 point [8]. Additionally, a spacecraft at the L_4 or L_5 point would obtain a side view from events like solar flares and CMEs which would help in developing a better understanding of these events as

1

well as the magnetic reconnection that triggers them [7]. Another interesting application of orbits around the equilateral points resides in their stability. The equilateral points are stable [9], which means that bodies in orbit around these points are likely to have been there for a long time. The study of asteroids in orbits around these Lagrange points can therefore help in understanding the formation of the Solar System. Such asteroids are generally called Trojans and they have been found in orbits around the equilateral points in the Sun-Mars, Sun-Earth, Sun-Jupiter and Sun-Neptune as well as around the equilateral points of Saturn with some of its moons. At the Sun-Earth L_4 point, one Trojan was discovered in 2010 with NASA's WISE spacecraft [10]. Detecting Trojans from Earth is challenging, as they appear very close to the Sun. It is therefore necessary to travel to these points to find out if there are other Trojans. The STEREO spacecraft visited both equilateral points in 2009 without spotting any Trojan and then in 2010, the only one known was discovered. This fact shows that there could still be other asteroids of small size or low albedo which have so far not been discovered [10]. Overall, the L_5 region is an interesting target for space missions.

In terms of propulsion, an electric low-thrust or chemical approach could be selected, but the use of a solar sail offers a novel method. Besides, since a solar-sail spacecraft can be propelled during its whole operational life, missions that would require too much propellant for an electric low-thrust approach could become possible. Previously, the NASA Sunjammer solar-sail mission was proposed to target an artificial L_1 point in the Sun-Earth system displaced towards the Sun to increase the warning time in case of solar events [11]. Unfortunately, the mission was cancelled. Part of the research contained in this report was conducted at NASA Marshall Space Flight Center showing that the interest of using solar sails to visit the Lagrange points goes beyond theory.

1.3. PREVIOUS WORK

The scientific interest in missions to the L_5 region has motivated a variety of studies demonstrating the feasibility of such a mission. For instance, transfers departing from a 200 km altitude Earth parking orbit and arriving to pre-selected orbits around the L_5 point have been found which require a $\Delta V \approx 4$ km/s; depending on the desired time of flight and the arrival orbit [7, 12]. Solar sails have proven to be excellent means to achieve a high ΔV [2]; in fact, for such a mission scenario, the use of a solar sail can decrease the total ΔV required [13]. For the work presented in Ref. [13], the invariant manifolds of planar Lyapunov orbits in the vicinity of Earth as well as differential correction and optimisation was used. Alternativelly, Ref. [14] used Poincaré sections to get initial guesses which were optimised for transfers between the collinear equilibrium points and the regions of practical stability around the L_4 and the L_5 points.

This thesis generalises the previous work by considering the three-dimensional case and a variety of invariant objects for the departure and arrival conditions including equilibrium points, families of periodic and quasi-periodic orbits as well as the stable manifold of periodic orbits for the mission scenario where the solar-sail spacecraft is launched as a secondary payload of a primary mission targeting a halo orbit around the L_1 point. Previous work have studied solar-sail equilibrium points and families of periodic orbits [1, 2, 13, 15]; however, little work has been done on families of solar-sail quasi-periodic orbits. Poincaré sections over the center manifold by means of a center manifold reduction has shown the existence of solar-sail quasi-periodic orbits, but an explicit definition of the orbits is lacking [15].

1.4. RESEARCH OBJECTIVE

In order to study the departure and arrival conditions for an L_5 mission as well as the transfer trajectories, this thesis aims to meet the following research objectives:

A. Improve the understanding of solar-sail bounded motion in the Circular Restricted Three-Body Problem (CR3BP) with Solar Radiation Pressure (SRP) by surveying and studying the different types of invariant objects in the system.

B. Determine what transfers are achievable between invariant objects in the vicinity of Earth and the L_5 region by generating a versatile strategy to compute time-optimal transfers.

In order to fulfil the research objectives, a set of research questions has been formulated. The answers to these research questions intend to provide the necessary information to achieve the research objectives.

I. What kind of invariant objects exist in the CR3BP + SRP and what are their properties regarding existence, shape and stability?

II. What is the effect of the lightness number on the properties of the invariant objects found under I.?

III. What approach is capable of computing time-optimal transfers between the invariant objects found under I.?

IV. What are the departure and arrival invariant objects that result in the fastest transfers to the L_5 region?

1.5. REPORT OUTLINE

The scientific research and results of this master thesis are presented in the form of a journal article. The article first gives the motivation and a brief description of the work, followed by a section describing the dynamical system used in this study. The next section contains a description on how to compute invariant objects with consideration for their existence, shape and stability. Then, the strategy adopted for the design of transfers between different types of invariant objects is described. Finally, the results are presented followed by the conclusions drawn from the results. This report includes another conclusions section to reflect on the research objectives and provide recommendations for future work. Lastly, a section on verification and validation is included to guarantee the validity of the methodology, results and conclusions.

2

JOURNAL ARTICLE

Solar-Sail Invariant Objects in the Sun-Earth system and transfers to the L_5 region

Alvaro Fernandez Mora

Delft University of Technology

Abstract

The development of solar-sail technology in combination with the rising interest in a mission to the Sun-Earth L_5 region for heliophysics and the search for Trojan asteroids, raises the question of using solar sailing as the primary propulsion method to enable such a mission. This study therefore investigates different invariant objects and their properties in the neighbourhood of Earth and in the L_5 region that could be used as departure and arrival conditions: equilibrium points, families of periodic orbits and families of invariant tori as well as the stable manifold of periodic orbits. Then, transfers between these invariant objects are studied using a hybridisation of different trajectory design techniques. A multi-objective genetic algorithm is applied to obtain near-feasible initial guesses, which are transformed into feasible transfers using a differential correction method. Through a continuation on the fixed time of flight, the differential corrector is subsequently used to reduce the transfer time. A pseudospectral optimisation method is finally taken at hand to obtain a smooth, continuous control profile, to, if possible, further reduce the transfer time. This approach results in fast solar-sail transfers between 391 and 1194 days, depending on the departure and arrival configuration and the assumed solar-sail technology. These results can serve as preliminary design solutions for a mission to the Sun-Earth L_5 region.

Keywords: Solar sails, periodic orbits, quasi-periodic orbits, L_5 mission, Trajectory optimisation

1. Introduction

The equilateral libration points of the Sun-Earth system are of interest for space missions related to space weather observations and the search for Trojan asteroids. Since these points are stationary 60 degrees ahead and behind Earth, they provide observational access to regions of the Sun that are inaccessible from Earth or the L_1 point. For example, the ACE satellite at the L_1 point allows the detection of geomagnetic storms approximately one hour before they arrive at Earth. A spacecraft at the equilateral points would enable a much earlier prediction of such space weather events. Furthermore, both equilateral points (L_4 and L_5) are suitable for studying coronal mass ejections (CMEs). However, only the L_5 point is useful for the study of corotating interaction regions as they pass by the L_5 region first, then Earth and lastly the L_4 region. Additionally, a spacecraft at the L_4 or L_5 points enables a side view of events like solar flares and CMEs which would help in developing a better understanding of these events as well as the magnetic reconnection that triggers them [1].

Apart from space weather observation missions, the equilateral points are also of interest because of the potential presence of Trojan asteroids. Bodies in orbit around the L_4 and L_5 points are likely to have been there for a long time due to the stable character of the orbits. The study of such bodies can therefore help in understanding the formation of the Solar System. Trojan asteroids have been found in orbit around the equilateral points of the Sun-Mars, Sun-Earth, Sun-Jupiter, and Sun-Neptune systems as well as in systems such as Saturn with some of its moons [2]. In 2010, NASA's WISE spacecraft detected asteroid 2010TK$_7$ at the Sun-Earth L_4 point [2]. The fact that the STEREO spacecraft visited both equilateral points a year before, in 2009, without spotting asteroid 2010TK$_7$ suggests that there could still be other asteroids of small size or low albedo which have yet not been discovered [2].

Due to the clear scientific relevance of the L_5 point, the literature holds a range of studies on transfers to the vicinity of this point. For example, studies have shown the feasibility of transfers departing from 200 km altitude parking

orbits around Earth to specific periodic orbits around the L_5 point. These transfers require a ΔV of the order of 4 km/s, depending on the targeted periodic orbit and the desired time of flight [3, 4]. Solar sails are an excellent means to provide this high ΔV [5]. As an inexhaustible source of low thrust, it can significantly decrease, if not completely remove, the need for onboard propellant. Moreover, Ref. [6] showed how, by using the invariant manifolds of planar Lyapunov orbits in combination with differential correction and optimisation, the use of a solar sail decreases the total ΔV for such a mission. Alternatively, Ref. [7] used Poincaré sections and optimal control to compute solar-sail transfers between the Sun-Earth collinear equilibrium points in the vicinity of Earth and the regions of practical stability around the equilateral libration points.

This paper builds on, and generalises, previous work on solar-sail transfers to the Sun-Earth L_5 region. In particular, a versatile approach is adopted to obtain solar-sail transfers departing from a range of natural and solar-sail invariant objects in the neighbourhood of Earth to entire families of periodic and quasi-periodic orbits in the L_5 region. The invariant objects considered are equilibrium points and families of periodic and quasi-periodic orbits. While previous work mostly focused on the planar, two-dimensional case and targeted specific initial and final conditions (e.g., a specific Earth parking orbit or a specific L_5 point orbit), this paper considers the three-dimensional case as well as entire families of periodic and quasi-periodic orbits for both the initial and final conditions.

2. Dynamical system

In order to model the motion of the solar-sail propelled spacecraft (hereafter in short referred to as "solar sail"), we consider the Circular Restricted Three-Body Problem (CR3BP) perturbed with Solar Radiation Pressure (SRP). In such a model, the Sun and the Earth (primary bodies) move in circular orbits around their common barycenter exclusively attracting each other. The solar-sail (third body) motion is governed by the vector field induced by the

3

gravitational pull of the primaries and the SRP. The primaries are assumed to be point masses and the solar sail is assumed to be massless.

The units of mass, distance and time are normalised such that the total mass of the system is 1, the Sun-Earth distance is 1 and the orbital period of the Earth around the Sun is 2π. With these normalised units, the gravitational parameter of Earth is $\mu = 3.0034806 \cdot 10^{-6}$ and the gravitational parameter of the Sun is $1 - \mu$.

We consider a synodic reference frame to study the system, where the origin is at the Sun-Earth barycenter, the $x-$axis is defined along the Sun-Earth line pointing from the Sun to the Earth, the $z-$axis is defined in the direction of the angular momentum vector of the primaries and the $y-$axis completes the orthogonal right-handed reference frame, see Fig. 1. In this frame, the equations of motion can be obtained by including the inertial and non-inertial accelerations as:

$$\ddot{x} - 2\dot{y} = \frac{\partial \Omega}{\partial x} + a_x, \tag{1}$$

$$\ddot{y} + 2\dot{x} = \frac{\partial \Omega}{\partial y} + a_y, \tag{2}$$

$$\ddot{z} = \frac{\partial \Omega}{\partial z} + a_z, \tag{3}$$

with $\Omega = \frac{1}{2}\left(x^2 + y^2\right) + \frac{1-\mu}{r_{sb}} + \frac{\mu}{r_{eb}}$, $r_{sb} = \sqrt{(x+\mu)^2 + y^2 + z^2}$ and $r_{eb} = \sqrt{(x+\mu-1)^2 + y^2 + z^2}$. Note that r_{sb} and r_{eb} are the norms of the Sun-body vector, $\boldsymbol{r}_{sb} = [x+\mu \quad y \quad z]^T$, and of the Earth-body vector, $\boldsymbol{r}_{eb} = [x+\mu-1 \quad y \quad z]^T$, respectively. The acceleration generated by the solar sail is defined as the vector $\boldsymbol{a} = [a_x \quad a_y \quad a_z]^T$ and is produced by the transfer of momentum when solar photons are reflected by the sail. In this process, the properties of the sail and the solar flux determine how the force is produced. For the initial analyses in this work, we assume a perfectly reflecting flat sail and a uniformly radiating Sun. Note that more complex models exist that account for the non-specular optical properties of the sail and geometry effects [5, 8, 9], but these are not considered in this work. For an ideal sail, the SRP acceleration acts along the direction of the sail normal and is conveniently expressed

4

as a function of the lightness number β. This parameter is defined as the ratio between the SRP and solar-gravitational accelerations [5]. Note that near-term values for this lightness number are $\beta \leq 0.04$ [10]. The SRP acceleration can then be described in dimensionless units as:

$$\boldsymbol{a} = \beta \frac{1-\mu}{r_{sb}^2} \langle \hat{\boldsymbol{r}}_{sb}, \boldsymbol{n} \rangle^2 \boldsymbol{n}, \tag{4}$$

where $\hat{\boldsymbol{r}}_{sb} = \frac{\boldsymbol{r}_{sb}}{r_{sb}}$ and $\boldsymbol{n}$ is the sail normal unit vector, see Fig. 1.
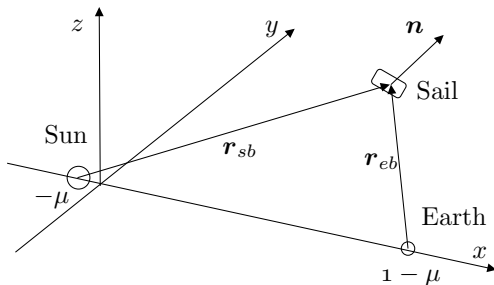
Figure 1: Sketch of the synodic reference frame.

In order to describe the attitude of the sail in the synodic frame, we follow Ref. [11] and define an orthonormal reference frame with its origin at the solar sail and basis $\{\hat{\boldsymbol{r}}_{sb}, \boldsymbol{p}, \boldsymbol{q}\}$, where $\boldsymbol{p} = \frac{\hat{\boldsymbol{r}}_{sb} \times \boldsymbol{k}}{|\hat{\boldsymbol{r}}_{sb} \times \boldsymbol{k}|}$ and $\boldsymbol{q} = \frac{\boldsymbol{p} \times \hat{\boldsymbol{r}}_{sb}}{|\boldsymbol{p} \times \hat{\boldsymbol{r}}_{sb}|}$. The vector $\boldsymbol{k}$ denotes the unit vector along the z-axis. The sail normal can then be described in the orthonormal frame by two angles, known in the literature as the cone angle α and the clock angle δ, as $\boldsymbol{n} = \cos\alpha \hat{\boldsymbol{r}}_{sb} + \sin\alpha \sin\delta \boldsymbol{p} + \sin\alpha \cos\delta \boldsymbol{q}$. Figure 2 shows the orthonormal reference frame centred at the solar-sail propelled spacecraft as well as the definition of the cone and clock angles.

The equations of motion can then be expressed as:

$$\ddot{x} - 2\dot{y} = \frac{\partial \tilde{\Omega}}{\partial x} + a\left(-\frac{(x+\mu)z}{r_{sb}r_p}\sin\alpha\cos\delta + \frac{y}{r_p}\sin\alpha\sin\delta\right), \tag{5}$$

$$\ddot{y} + 2\dot{x} = \frac{\partial \tilde{\Omega}}{\partial y} + a\left(-\frac{yz}{r_{sb}r_p}\sin\alpha\cos\delta - \frac{x+\mu}{r_p}\sin\alpha\sin\delta\right), \tag{6}$$

$$\ddot{z} = \frac{\partial \tilde{\Omega}}{\partial z} + a\left(\frac{r_p}{r_{sb}}\sin\alpha\cos\delta\right), \tag{7}$$

5
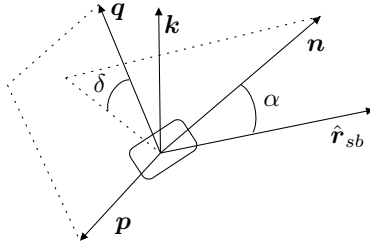
Figure 2: Sketch of the local frame used to define the cone angle α and the clock angle δ.

where $r_p = \sqrt{(x+\mu)^2 + y^2}$, $\tilde{\Omega} = \frac{1}{2}\left(x^2 + y^2\right) + \left(1 - \beta\cos^3\alpha\right)\frac{1-\mu}{r_{sb}} + \frac{\mu}{r_{eb}}$ and $a = \beta\frac{1-\mu}{r_{sb}^2}\cos^2\alpha$. The right-hand side of Eqs. 5-7 consist of terms of two different nature, where the terms associated with $\tilde{\Omega}$ accept the form of a potential function. While the CR3BP is Hamiltonian, the SRP perturbation breaks this property of the system, although a few exceptions exist. For the cases where the non-potential terms on the right-hand side of Eqs. 5-7 vanish, the system remains Hamiltonian. This happens when the sail normal is aligned with the direction of the Sun-sail line ($\alpha = 0$) and when the sail normal is perpendicular to the Sun-sail line ($\alpha = \pm\pi/2$). For these cases, the existence of periodic and quasi-periodic motion around the equilibrium points is guaranteed [11]; therefore, they are of particular interest. Another important aspect of the dynamical system when the Hamiltonian structure is preserved is the existence of a first integral $J_c = \dot{x}^2 + \dot{y}^2 + \dot{z}^2 - 2\tilde{\Omega}$, known as the Jacobi constant [11]. This constant of motion has important implications for the characterisation of regions of possible motion and energy levels of periodic and quasi-periodic orbits.

3. Invariant objects

Let us express Eqs. 5-7 as a system of first order differential equations given by:

$$\dot{\boldsymbol{x}} = f(\boldsymbol{x}, \alpha, \delta), \tag{8}$$

where $\boldsymbol{x} \in \mathbb{R}^6$ belongs to the phase space of the configuration system, $\alpha \in [-\pi/2, \pi/2]$ and $\delta \in [0, \pi]$. Let us also define the flow induced by f as $\phi_t(\boldsymbol{x}, \alpha, \delta)$

6

with $t \in \mathbb{R}$. A set $\mathcal{S} \subset \mathbb{R}^6$ is invariant under the flow if for any element $\boldsymbol{x} \in \mathcal{S}$, $\phi_t(\boldsymbol{x}, \alpha, \delta) \in \mathcal{S}$ for any t [12]. When the angles α and δ are constant, they act simply as parameters of the dynamics for which invariant sets can be defined. A wide variety of invariant objects exist in both the natural CR3BP and CR3BP-SRP including equilibrium points, periodic orbits, invariant manifolds and invariant tori. Regarding periodic orbits, this article focuses on the planar and vertical Lyapunov families as well as the halo families.

3.1. Equilibrium points

It is well know that the CR3BP exhibits five equilibrium points known as the Lagrange points. The linear dynamics of the collinear equilibrium points are of type saddle×centre×centre, whereas for the equilateral Lagrange points they are of type centre×centre×centre. Therefore, the collinear Lagrange points are linearly unstable because of the saddle and the equilateral points are linearly stable. In the CR3BP-SRP, 3-dimensional equilibrium surfaces exist [5, 11]. The surfaces of these so-called displaced equilibrium points are given by the following problem [5]:

$$-\nabla\Omega = \beta\frac{1-\mu}{r_{sb}^2}\langle\hat{\boldsymbol{r}}_{sb}, \boldsymbol{n}\rangle^2\boldsymbol{n}, \tag{9}$$

$$\langle\hat{\boldsymbol{r}}_{sb}, \boldsymbol{n}\rangle \geq 0. \tag{10}$$

Note that, when the sail normal is perpendicular to the Sun-sail line, which would be equivalent to $\beta = 0$, the displaced equilibrium points reduce to the five Lagrange points. On the other hand, when the sail normal is oriented parallel to the Sun-sail line, five displaced counterparts of the Lagrange points exist. These equilibrium points are referred to as SL_i with $i \in \{1, 2, .., 5\}$. Sections of the surface of equilibria can be obtained with a continuation of the solutions from the already known equilibrium points, i.e., the (displaced) Lagrange points. Note that for each of the equilibrium points forming the surfaces of equilibria the cone and clock angle are fixed.

7

The stability of the displaced equilibrium points can also be studied by examining the linearised dynamics. Following Ref. [11], we distinguish three types of equilibrium points according to their linear stability:

- $\mathcal{T}_1$: Equilibrium points with eigenvalues $\lambda_1 > 0, \lambda_2 < 0, \lambda_{3,4} = u_1 \pm iv_1, \lambda_{5,6} = u_2 \pm iv_2$. Additionally $|u_{1,2}| < |\lambda_{1,2}|$. This type represents unstable equilibria where the instability comes mainly from the saddle.

- $\mathcal{T}_2$: Equilibrium points with all eigenvalues complex $\lambda_{1-6} = u_{1,2,3} \pm v_{1,2,3}$ and $|u_i| > 0.001$ for some $i \in \{1, 2, 3\}$. This type represents unstable equilibria where the instability comes from a complex saddle.

- $\mathcal{T}_3$: Equilibrium points with all eigenvalues complex $\lambda_{1-6} = u_{1,2,3} \pm v_{1,2,3}$ and $|u_i| < 0.001$ for $i \in \{1, 2, 3\}$. This type represents stable ($u_i = 0$) and almost stable ($|u_i| \in (0, 0.001]$) behaviour given by centres and weak complex saddles, respectively.

Figure 3 shows the intersection of the surfaces of equilibria with the ecliptic plane for $\beta \in \{0.01, 0.02, ..., 0.05\}$ and their stability classification. For $\beta \in \{0.01, 0.02\}$, there are three surfaces; two isolated around L_1 and L_2 and another one containing $L_{3,4,5}$. For $\beta > 0.02$, the surface around L_1 and the surface containing $L_{3,4,5}$ merge into one torus-like surface while the surface around L_2 remains. For a more detailed analysis on the behaviour of the surface of equilibria with β, the reader can consult Ref. [11]. Regarding stability, the equilibrium points around the collinear Lagrange points are of type $\mathcal{T}_1$, i.e., unstable. In the neighbourhood of Earth, there are regions of equilibrium points of type $\mathcal{T}_2$ and therefore unstable because of the complex saddle. Lastly, part of the torus-like surface containing the triangular Lagrange points is of type $\mathcal{T}_3$ and therefore, stable and almost stable. The lightness number alters the surfaces of equilibria, but the stability classification of the equilibrium points does not show much of a change.
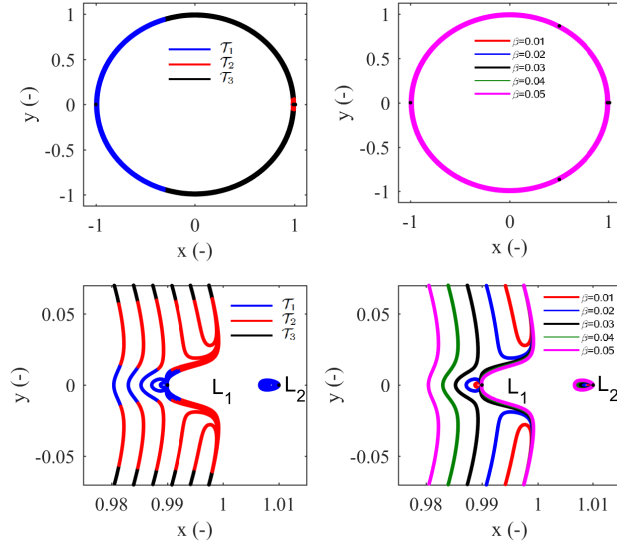
Figure 3: Sections of the surfaces of equilibria in the ecliptic plane and their stability classification for $\beta \in \{0.01, 0.02, ..., 0.05\}$ (top) and close-up in the neighbourhood of Earth (bottom).

3.2. Periodic orbits

When the dynamical system is Hamiltonian, both periodic and quasi-periodic motion around the equilibrium points exist. In fact, these types of orbits generally appear in continuous families. Numerous studies have used symmetric properties of the system to compute such families of periodic orbits in the natural system, e.g., [13, 14], and the SRP-perturbed system, e.g., [15, 16]. We, however, do not exploit orbit symmetry to find periodic orbits. A very general way to impose periodic motion is given by the definition of the map $G : \mathbb{R}^7 \to \mathbb{R}^6$ as [17]

$$G(\boldsymbol{x}, T) = \phi_T(\boldsymbol{x}, \alpha, \delta) - \boldsymbol{x}. \tag{11}$$

Note that the sail attitude is constant for each family of periodic orbits and therefore α and δ are fixed parameters of the map G. The search for periodic orbits is then transformed into finding $\{\boldsymbol{x}, T\}$ that solve $G(\boldsymbol{x}, T) = 0$. Such solutions can be found with a Newton method given a good initial guess.

9

Let us assume $\{\hat{\boldsymbol{x}}, \hat{T}\}$ is a guess for a solution. This guess can be corrected by linearising the periodicity equation and solving the linear system, i.e.,

$$-G(\hat{\boldsymbol{x}}, \hat{T}) = JG(\hat{\boldsymbol{x}}, \hat{T}) \begin{bmatrix} \delta\boldsymbol{x} \\ \delta T \end{bmatrix}, \qquad (12)$$

where JG denotes the Jacobian of G and $\delta\boldsymbol{x}$ and δT denote the updates to the initial guess. The derivative of $\phi_T(\boldsymbol{x}, \alpha, \delta)$ with respect to the initial point $\boldsymbol{x}$ can be obtained with the state transition matrix (STM) evaluated at time T denoted by $\Phi(\boldsymbol{x}, T, \alpha, \delta)$, which is referred to as the monodromy matrix, yielding

$$JG = \Big[\Phi(\boldsymbol{x}, T, \alpha, \delta) - I_{6\times6} \quad f(\phi_T(\boldsymbol{x}, \alpha, \delta), \alpha, \delta) \Big], \qquad (13)$$

where $I_{6\times6}$ denotes the identity matrix. The matrix JG is of size 6×7 and is therefore not invertible. However, it is convenient to fix one of the components, x_i, of $\boldsymbol{x}$ to have control in the continuation of the families of periodic orbits. To do so, it is enough to set its variation δx_i to zero in Eq. 12, which is equivalent to eliminating δx_i from the updates vector and eliminating column i from JG, yielding the reduced Jacobian $\tilde{J}G$. The system can then be solved by inverting $\tilde{J}G$.

3.2.1. Continuation of the families of periodic orbits

Let us define the reduced vector $\tilde{\boldsymbol{x}}$ as the vector $\boldsymbol{x}$ without the x_i component. Then, the map $G(\boldsymbol{x}, T)$ can be rewritten as $G(\tilde{\boldsymbol{x}}, T, x_i)$. Let us also assume $\{\tilde{\boldsymbol{x}}^*, T^*, x_i^*\}$ is a solution. The implicit function theorem guarantees that as long as $det\left(\frac{\partial G(\tilde{\boldsymbol{x}}^*, T^*, x_i^*)}{\partial \tilde{\boldsymbol{x}}, T}\right) \neq 0$, there exists a neighbourhood around the solution where the functions $\tilde{\boldsymbol{x}}(x_i)$ and $T(x_i)$ exist and $G(\tilde{\boldsymbol{x}}(x_i), T(x_i), x_i) = 0$ in that neighbourhood. By implicit differentiation of G with respect to x_i, it is possible to obtain the unit tangent direction for a family of periodic orbits, $\bar{\boldsymbol{t}}$, as the unit $Ker(JG(\boldsymbol{x}^*, T^*))$. The initial guess for the next orbit in the family is then obtained as [18]:

$$\begin{bmatrix} \hat{\boldsymbol{x}} \\ \hat{T} \end{bmatrix} = \begin{bmatrix} \boldsymbol{x}^* \\ T^* \end{bmatrix} + \delta S \bar{\boldsymbol{t}}, \qquad (14)$$

10

where δS is the step size in the continuation and the next solution is computed at the fixed value of $x_i = x_i^* + \delta S \bar{t}_i$.

In order to implement this method for the generation of families of periodic orbits, initial guesses for the first orbits in the families are required. We obtained these guesses from the oscillatory modes of the linearised flow at the equilibrium points.

3.2.2. Orbit stability

An important feature of periodic orbits is their stability, which can be assessed from the eigenvalues of the monodromy matrix. Since we will only generate periodic orbits for the Hamiltonian case ($\alpha = 0$ or $\alpha = \pm \pi/2$), the monodromy matrix is symplectic. It can be shown that the characteristic polynomial of any symplectic matrix is reciprocal and consequently, the roots come in reciprocal pairs. Therefore, if λ is an eigenvalue, λ^{-1} is also an eigenvalue. It can also be shown that for periodic orbits in autonomous Hamiltonian systems, one of the eigenvalues is equal to 1 with an associated eigenvector tangent to the orbit. Since the eigenvalues come in reciprocal pairs, the spectra of the monodromy matrix has the form [19]:

$$spec(M) = \{1, 1, \lambda_1, \lambda_1^{-1}, \lambda_2, \lambda_2^{-1}\}. \tag{15}$$

The stability indices are then defined as $s_i = |\lambda_i + \lambda_i^{-1}|$. With such definition, a periodic orbit can be described as [20]:

- Hyperbolic: $s_i > 2$.

- Elliptic: $s_i \leq 2$. When $s_i = 2$ it is also said to be parabolic.

- Complex unstable: if $\lambda_i \in \mathbb{C} \backslash \mathbb{R}$ and $|\lambda_i| \neq 1$

A periodic orbit is said to be stable if $s_i \leq 2$ for $i \in \{1, 2\}$ [20].

In this paper we consider only the planar Lyapunov, vertical Lyapunov and halo families, but several other exist [21]. In order to study the evolution of the stability of the orbits within each family and the effect of the lightness number,

we compare the stability indices in logarithmic scale against a normalised Jacobi constant j_c for each orbit within the families. The normalised Jacobi constant is defined as the Jacobi constant divided by the maximum absolute value of the Jacobi constant encountered in each family. The use of the normalised Jacobi constant is convenient for comparing the stability indices of families at different lightness number since it is a variable with the same bounds for all β; therefore, all stability curves can be represented together in a clear way. Generally, for the families considered in this study, the Jacobi constant (and also j_c) increase throughout the continuation; therefore, the lowest value of j_c is found for the orbits close to the equilibrium point, i.e., the orbits at the start of the families, and as the families are continued, they increase in j_c. This general rule applies for the planar and vertical Lyapunov families around the (displaced) L_1 and L_2 points and for the halo families around the (displaced) L_1 point.

3.2.3. Planar Lyapunov families in the vicinity of Earth

In order to detect changes in the shape of the families with the lightness number, we consider different geometric comparisons specific to each family. We first study the planar Lyapunov families around the (displaced) L_1 and L_2 points for which the following sections are defined [20]:

$$\Lambda_1 = \{y = 0, \dot{y} > 0\} \tag{16}$$

$$\Lambda_2 = \{y = 0, \dot{y} < 0\}. \tag{17}$$

For the planar Lyapunov families around the (displaced) L_1 point, we compute the maximum y value, y_{max} for each orbit within the family and plot it against the difference $d(SL_1)$ between the intersection with Λ_1 and the (displaced) L_1 point. For the planar Lyapunov families around the (displaced) L_2 point, we proceed in the same way but using the section Λ_2. Figure 4 shows the intersections with Λ_1 and Λ_2 for a orbit around SL_1 as well as the variables $d(SL_1)$ and y_{max}.

As an example, Fig. 5 shows the planar Lyapunov families around the SL_1 point (left) and the SL_2 point (right) for $\beta = 0.04$. The drift of the
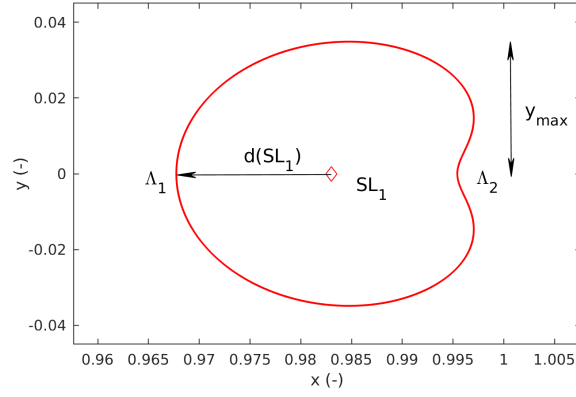
Figure 4: Intersections with Λ_1 and Λ_2 for a planar Lyapunov orbit around SL_1 as well as variables $d(SL_1)$ and y_{max}.

intersection with Λ_1 and Λ_2 for both families can clearly be appreciated, where the intersection moves towards the Sun for the family around the SL_1 point, whereas for the family around SL_2 it first moves away from Earth and then towards.
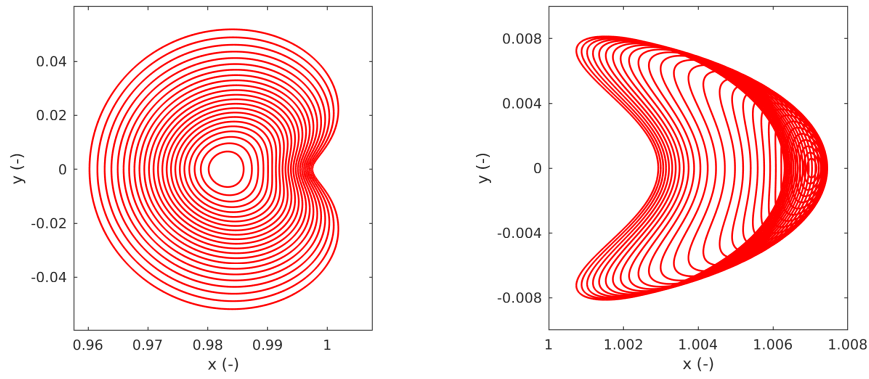
Figure 5: Planar Lyapunov families around the SL_1 point (left) and the SL_2 point (right) for $\beta = 0.04$.

Figure 6 shows the results for the geometric comparison for the families around the (displaced) L_1 point (left) and the (displaced) L_2 point (right) for

$\beta \in \{0, 0.01, ..., 0.05\}$. Note that the orientation of the orbits that belong to these families is clockwise when seen from $z > 0$. It can be seen that for the orbits around the (displaced) L_1 point, the intersection with Λ_1 moves towards the Sun for all lightness numbers and the orbits increase y_{max} within a family. Furthermore, the larger β, the smaller the maximum y value for the same $d(SL_1)$. Therefore, the orbits become closer to $y = 0$ for increasing β. The planar Lyapunov families around the (displaced) L_2 point experiences a change in behaviour with β. For $\beta \leq 0.01$, the intersection always occurs for positive $d(SL_2)$, whereas for $\beta \geq 0.03$ it first occurs for positive $d(SL_2)$ and then negative. Lastly, for $\beta = 0.02$ the intersection with Λ_2 alternates between positive and negative $d(SL_2)$. Furthermore, for $\beta \leq 0.03$, the orbits always increase y_{max} along a single family, while for $\beta \geq 0.04$, it starts decreasing at some point in the family.
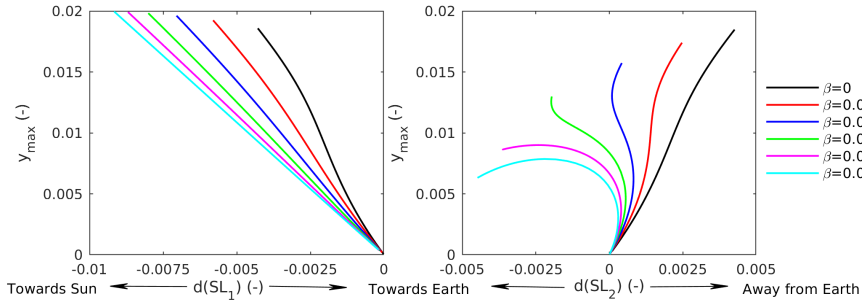
Figure 6: Planar Lyapunov families around the (displaced) L_1 and L_2 points: y_{max} against $d(SL_1)$ for the families around the (displaced) L_1 (left) and against $d(SL_2)$ for the families around the (displaced) L_2 (right) for $\beta \in \{0, 0.01, ..., 0.05\}$.

Regarding the stability of the planar Lyapunov families, Fig. 7 shows both stability indices for the families around the (displaced) L_1 and L_2 points against j_c. The figure shows that $s_1 > 2$ for both families and they are therefore unstable for the lightness numbers considered. The orbits at the smallest values for j_c, which exist at the start of the family, have a central part, i.e., $s_2 = 2$. When the orbits increase their Jacobi constant, sets of orbits that do not posses a centre manifold emerge where $s_2 \neq 2$.

14
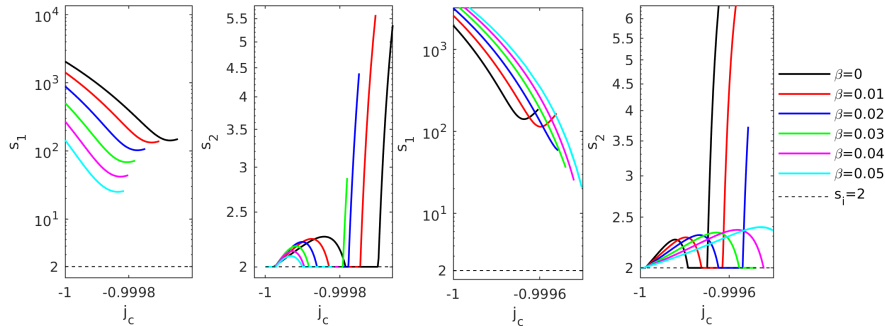
Figure 7: Planar Lyapunov families around the (displaced) L_1 and L_2 points: Stability indices s_1 and s_2 in logarithmic scale for the families around the (displaced) L_1 point (left) and the (displaced) L_2 point (right) for $\beta \in \{0, 0.01, ..., 0.05\}$.

3.2.4. Vertical Lyapunov families in the vicinity of Earth

The vertical Lyapunov family is the second type of orbits that originate from the collinear equilibrium points. For the geometric comparison of the families with β, we compute the maximum z value, z_{max}, of the orbits and plot z_{max} against the maximum y value, y_{max}. As an example, Fig. 8 shows the vertical Lyapunov families around the SL_1 point (left) and around the SL_2 point (right) for $\beta = 0.04$. It can be seen that for the vertical Lyapunov orbits around the SL_1 point, the orbits increase z_{max} along the family. Furthermore, some orbits that present an extra loop appear, but such extra loop is subsequently lost. One such orbit is depicted in black in Fig. 8 (left). For the family around the SL_2 point, a range of orbits where the maximum altitude with respect to the ecliptic decreases with increasing y_{max} to then start increasing again can be appreciated.

Figure 9 shows the results obtained for the geometric comparison. The families around the (displaced) L_1 point all follow the same trend; the larger y_{max} the further they extend out of the ecliptic. Furthermore, increasing the lightness number pushes the orbits towards $y = 0$. For the families around the (displaced) L_2 point, when $\beta \leq 0.03$, the orbits increase z_{max} with increasing y_{max}, whereas for $\beta > 0.03$ there is a change in this trend. For $\beta = 0.04$, a

15
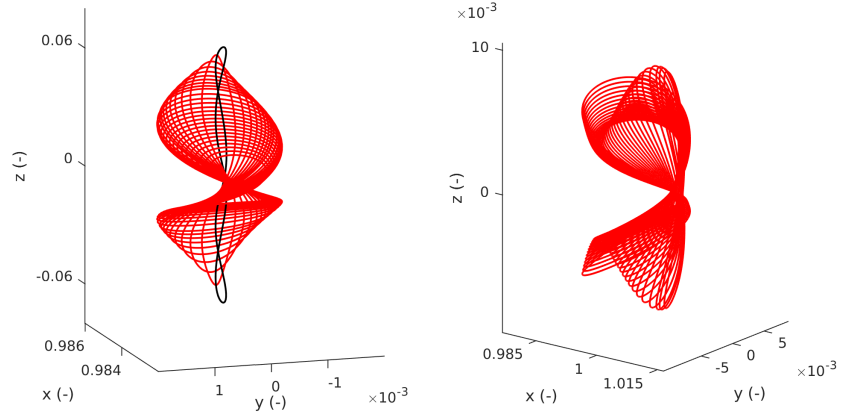
Figure 8: Vertical Lyapunov families around the SL_1 point (left) and around the SL_2 point (right) for $\beta = 0.04$.

range of orbits exists that decreases their maximum altitude above the ecliptic for increasing y_{max}. For $\beta = 0.05$ the orbits even bifurcate to planar orbits.
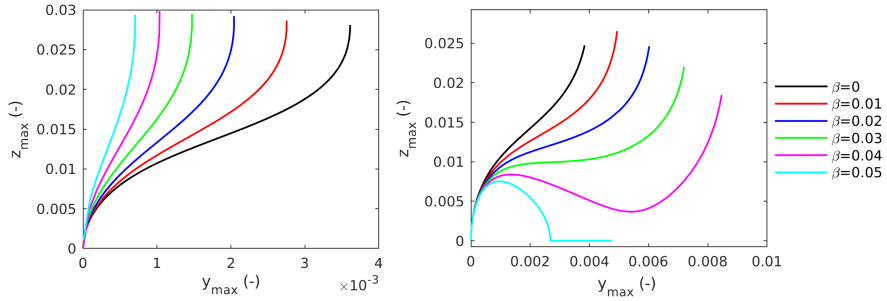
Figure 9: Vertical Lyapunov families around the (displaced) L_1 and L_2 points: z_{max} against y_{max} for the families around the (displaced) L_1 point (left) and the (displaced) L_2 point (right) for $\beta \in \{0, 0.01, ..., 0.05\}$.

The stability indices for these families are shown in Fig. 10. The families around both the (displaced) L_1 and L_2 points are unstable since no orbit exists with $s_i = 2$ for $i = 1, 2$. Note that for the family around SL_2 and $\beta = 0.05$, when $s_1 = 2$, $s_2 \neq 2$. In fact, such a case corresponds to the bifurcation point where the vertical Lyapunov orbits become planar. The orbits around the (displaced)

16

$L_{1,2}$ points at the start of the families, where $j_c \approx -1$, have a central part that is eventually lost when the Jacobi constant increases where $s_2 \neq 2$.
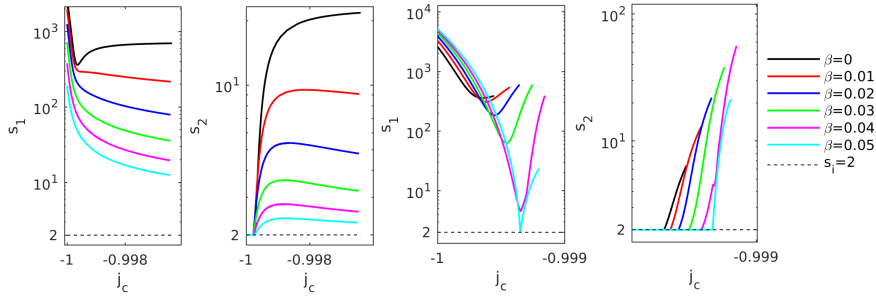
Figure 10: Vertical Lyapunov families around the (displaced) L_1 and L_2 points: stability indices s_1 and s_2 in logarithmic scale for the families around the (displaced) L_1 point (left) and the (displaced) L_2 point (right) for $\beta \in \{0, 0.01, ..., 0.05\}$.

3.2.5. Halo families in the vicinity of Earth

When the non-linear effects become important, a new family known as the halo family bifurcates from the planar Lyapunov families around the collinear equilibrium points [22]. Such a family presents two branches: the northern and the southern halos. These branches are symetric with respect to the $z = 0$ plane. In this study we consider only the northern branch. In order to make a geometric comparison of the northern halo families around the (displaced) L_1 and L_2 points, we compute z_{max} and plot it against $d(SL_1)$ or $d(SL_2)$, which in this case denotes the difference between the x value where z_{max} is reached and the x value of the associated equilibrium point of the family. As an example, Fig. 11 shows the northern halo families around the SL_1 point (left) and the SL_2 point (right) for $\beta = 0.04$. The change in the shape with respect to the natural halo family around SL_1 can clearly be seen as the family collapses onto the ecliptic instead of finishing in near rectilinear halo orbits.

Figure 12 shows the results obtained for the geometric comparison for $\beta \in \{0, 0.01, ..., 0.05\}$. For the families around the (displaced) L_1 point, it can be seen that a change in behaviour takes place for $\beta > 0.03$. For $\beta \leq 0.01$, the point

17
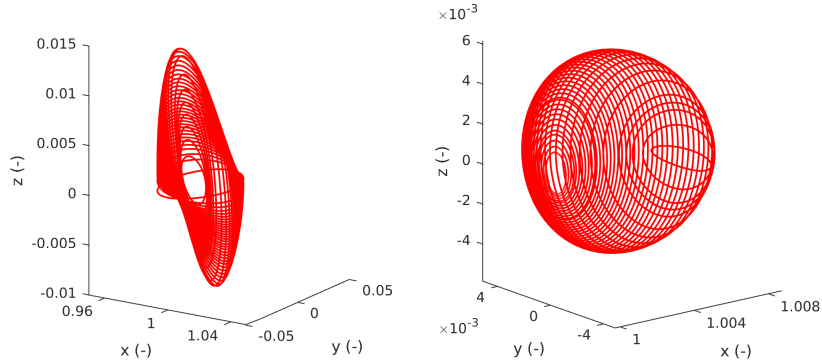
Figure 11: Northern halo families around the SL_1 point (left) and around the SL_2 point (right) for $\beta = 0.04$.

of maximum z value drifts in the direction of positive $d(SL_1)$ and further from the ecliptic plane throughout the families. For $\beta = 0.02$, it first moves in the direction of negative $d(SL_1)$ and then positive, but towards larger z values. For $\beta = 0.03$, the point of largest z value alternates between positive and negative $d(SL_1)$ and increasing and decreasing z_{max}. Lastly, for $\beta \geq 0.04$, the highest point always drifts towards the Sun, but z_{max} first increases and then decreases until the orbits become planar. It is known that, during the continuation of the halo family around SL_1 with β, there is a bifurcation at $\beta \approx 0.387$ which explains the change in behaviour between $\beta = 0.03$ and $\beta = 0.04$ [22]. In general, changes in the geometric behaviour of orbits within a type of family appear to occur for a lightness number somewhere between 0.03 and 0.04. This suggests that there is a lightness number $\beta^* \in (0.03, 0.04)$ for which the dynamics change qualitatively, at least in the vicinity of Earth. For the family around the (displaced) L_2 point, the highest point always drifts towards the Earth and z_{max} first increases and then decreases. Similar results were already observed for the halo families in Ref. [23].

Regarding stability, Fig. 13 shows the stability indices for the northern halo families around the (displaced) L_1 point (left) and the (displaced) L_2 point (right) for $\beta \in \{0, 0.01, ..., 0.05\}$. The northern halo families around the (dis-

18
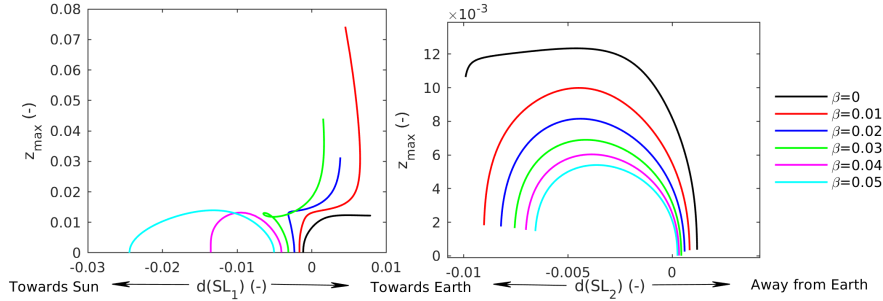
Figure 12: Northern halo families around the (displaced) L_1 and L_2 points: z_{max} against $d(SL_1)$ for the families around the (displaced) L_1 point (left) and against $d(SL_2)$ for the families around the (displaced) L_2 point (right) for $\beta \in \{0, 0.01, ..., 0.05\}$.

placed) L_2 point, as opposed to the planar and vertical Lyapunov families and the halo families around the (displaced) L_1 point, are families where the Jacobi constant first increases and then decreases. In fact, the smallest values of the Jacobi constant are reached for the orbits at the end of the families for $\beta \geq 0.01$. Therefore, the families for such lightness numbers end at $j_c = -1$. For $\beta = 0$, the smallest Jacobi constant is reached at the start of the family; thus, the family starts at $j_c = -1$. There are stable northern halo orbits around both the (displaced) L_1 and L_2 points as there are orbits with $s_1 = 2$ and $s_2 = 2$. For the families around the (displaced) L_2 point, these stable halo orbits emerge when the families approach near rectilinear halo orbits at the end of the families. Also, note that the orbits in the families around the (displaced) L_2 point always have a central part as $s_2 = 2$ for all β. Figure 13 also shows ranges of orbits with similar values of j_c where the stability indices intersect with $s_i = 2$ more than once, suggesting an interesting behaviour worth analysing in future work.

3.2.6. Lypunov families in the L_5 region

Lastly, two orbit families originate from the (displaced) L_4 and L_5 points: the planar and vertical Lyapunov families. For these two families, there is no notable change with the lightness number in the geometric behaviour so a

19
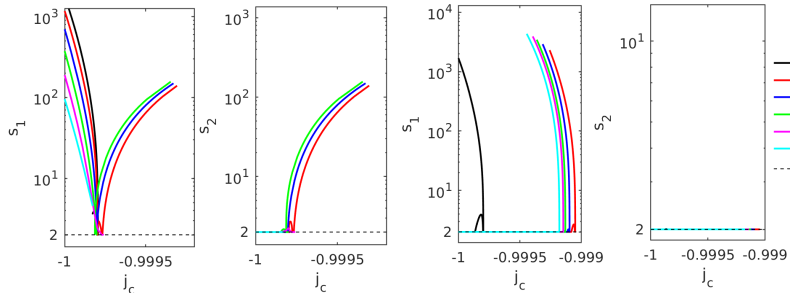
Figure 13: Northern halo families around the (displaced) L_1 and L_2 points: stability indices s_1 and s_2 in logarithmic scale for the families around the (displaced) L_1 point (left) and the (displaced) L_2 point (right) for $\beta \in \{0, 0.01, ..., 0.05\}$.

geometric comparison is not presented. Figure 14 shows the planar orbit (left) and the vertical orbit (right) around the SL_5 point for $\beta = 0.04$. These families are stable for all β since the orbits are always elliptic, i.e., $s_1 = 2$ and $s_2 = 2$.
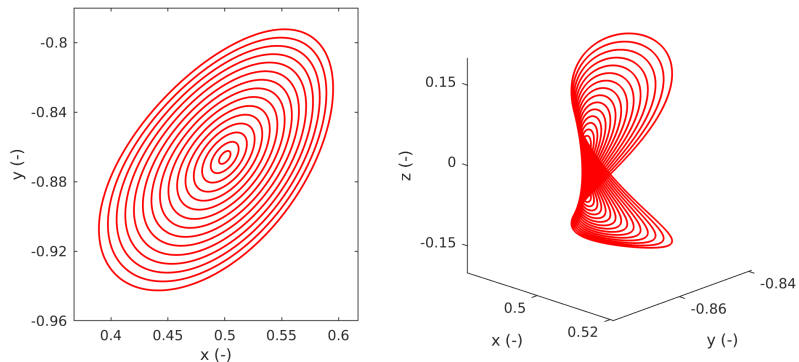
Figure 14: Planar (left) and vertical (right) Lyapunov families around the SL_5 point for $\beta = 0.04$.

3.3. Invariant Tori

A first integral can be seen as a functional F that is invariant under the flow. It can be shown that a first integral can also be described in terms of a Poisson

20

bracket. The Poisson bracket of two functions h_1 and h_2 is defined as [19]:

$$\{h_1, h_2\} = \nabla h_1^T J \nabla h_2 \tag{18}$$

where

$$J = \begin{bmatrix} 0 & I \\ -I & 0 \end{bmatrix}. \tag{19}$$

For a Hamiltonian dynamical system, let us denote the Hamiltonian by H. Then, a first integral is a functional h that satisfies $\{H, h\} = 0$. If two functions satisfy such condition, they are said to be in involution [24]. An important result, known as the Arnold-Liouville theorem, proves that for a system with a $2n$-dimensional phase space, if n independent first integrals F_i with $i \in \{1, 2, ..n\}$ exist, the system is integrable. Furthermore, let us define the set

$$M_f = \{\boldsymbol{x} : F_i(\boldsymbol{x}) = C_i, \quad i \in \{1, 2, ...n\}\}, \tag{20}$$

where C_i are constants. Assuming F_i are all independent on M_f, then M_f is a smooth manifold invariant under the flow with Hamiltonian H. Additionally, if M_f is compact and connected, it is diffeomorphic to the n-dimensional torus [24]. A corollary of the Arnold-Liouville theorem is that for an integrable system, bounded trajectories lie on a torus where both periodic and quasi-periodic orbits may exist. Neither the CR3BP nor the CR3BP + SRP are integrable, so the Arnold-Liuville theorem does not apply. Nevertheless, KAM theory shows that quasi-periodic motion does exist in these systems [25].

We explore 2-dimensional tori for the case where the dynamical system is Hamiltonian. Therefore, we are interested in a parameterisation $\psi : \mathbb{T}^2 \to \mathbb{R}^6$ such that [26]

$$\psi(\boldsymbol{\theta} + \boldsymbol{\omega} t) = \phi_t(\psi(\boldsymbol{\theta}), \alpha, \delta), \tag{21}$$

where $\boldsymbol{\theta} = [\theta_1 \quad \theta_2]^T \in \mathbb{R}^2$ parameterises the torus and $\boldsymbol{\omega} = [\omega_1 \quad \omega_2]^T \in \mathbb{R}^2$ is the vector of frequencies. Figure 15 depicts the torus domain together with a possible choice for θ_1 and θ_2 that is mapped to the quasi-periodic orbits under ψ. Instead of looking for a paramaterisation of the full torus, it is possible to reduce the dimension of the problem by looking for a paramaterisation of an
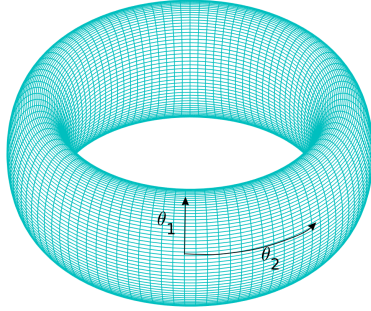
Figure 15: Representation of a torus and the variables θ_1 and θ_2.

invariant curve $\varphi : \mathbb{T}^1 \rightarrow \mathbb{R}^6$ under a stroboscopic map ϕ_{T_2}, where T_2 is the period associated with the frequency ω_2. The invariance condition for the curve under the map can be expressed as

$$\varphi(\xi + \rho) = \phi_{T_2}(\varphi(\xi), \alpha, \delta), \tag{22}$$

where ρ is the rotation number and ξ is the parameter that parameterises φ. Note that the rotation number and T_2 are related as $\rho = \omega_1 T_2$ [26].

A paramaterisation of the invariant curve can be obtained with complex truncated Fourier series as

$$\varphi(\xi) = \sum_{k \in K} \boldsymbol{c}_k e^{ik\xi}, \tag{23}$$

where K is an index set [27] and $\boldsymbol{c}_k$ are the complex Fourier coefficients. By discretising ξ into N values ξ_j with $j \in \{1, 2, ..., N\}$, it is possible to discretise the invariant curve into N points $\varphi(\xi_j)$. Consequently, by means of the discrete Fourier transform (DFT), there is a linear relation between the complex coefficients $\boldsymbol{c}_k$ of the Fourier series and the discretised invariant curve. Expressing the coefficients and the discretised curve as the column vectors $\boldsymbol{c}$ and $\boldsymbol{u}$, respectively, yields the relation [27]

$$\boldsymbol{c} = D\boldsymbol{u}, \tag{24}$$

where D is the linear operator for the DFT. In this study we use $N = 35$; therefore, the invariant curves are discretised into 35 points and expressed in Fourier

series up to degree 35. In order to meet the invariance condition expressed in Eq. 22, a rotation operator R is used to rotate the mapped curve under the stroboscopic map for an angle $-\rho$, i.e.,

$$R(-\rho) \circ \phi_{T_2}(\varphi(\xi), \alpha, \delta) - \varphi(\xi) = 0. \tag{25}$$

The rotation can be performed by first obtaining the Fourier coefficients of the mapped discretised curve, then transforming each coefficient with another operator $Q(-\rho) : \boldsymbol{c}_k \to \boldsymbol{c}_k e^{-ik\rho}$ and finally obtaining the states in the rotated curve. Consequently, $R(-\rho) = D^{-1}Q(-\rho)D$ [27].

To ensure that the invariant curve defines a quasi-periodic orbit, it is necessary that all points of the curve have the same Jacobi value. Therefore, each point of the invariant curve is constrained to

$$J_c(\varphi(\xi_j)) = J_c^{fixed}. \tag{26}$$

Given a good initial guess, the invariance condition from Eq. 25 together with the Jacobi constraint from Eq. 26 can be used in a Newton method to obtain invariant curves together with the rotation number ρ and the period T_2. Figure 16 shows a discretised guess $\hat{\varphi}(\xi)$ for an invariant curve and its image under the stroboscopic map (left) and the converged solution and its image (right) for a tolerance of 10^{-10} after three iterations. From the converged solution, it can be appreciated how the flow comes back to the same curve.

Given a periodic orbit defined by a phase space point $\boldsymbol{x}_p$ and a period T, if such an orbit is elliptic, i.e., at least one of its stability indices $s_i = 2$, then the eigenplane passing through $\boldsymbol{x}_p$ associated with the eigenvalues λ_i and λ_i^{-1} contains invariant curves of the linearisation around $\boldsymbol{x}_p$ of a stroboscopic map with stroboscopic time $T_2 = T$, i.e., the monodromy matrix. Some of these invariant curves subsist in the full system, giving rise to invariant tori around the periodic orbits [26]. Therefore, given λ_i an eigenvalue within the unit circle, and the associated complex eigenvector $\boldsymbol{y}$, the initial guess can be obtained as [27]

$$\hat{\varphi}(\xi) = \boldsymbol{x}_p + \rho_\epsilon[\cos(\xi)Re(\boldsymbol{y}) - \sin(\xi)Im(\boldsymbol{y})], \tag{27}$$

23
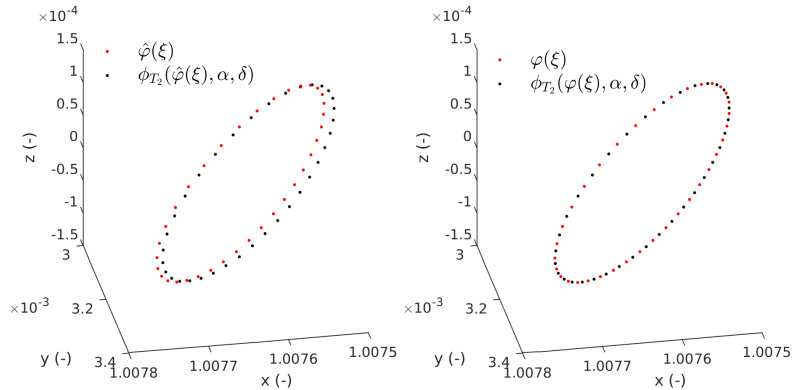
Figure 16: Guess for an invariant curve and its image under the stroboscopic map (left) and the converged solution and its image after three iterations (right).

where ρ_ϵ is the radius of the initial guess for the invariant curve taken as 10^{-7} dimensionless units. For the rotation number, it can be shown that the phase of λ_i can be used as an initial guess [27].

3.3.1. Continuation of the families of invariant tori

Once a solution has been found, it is possible to continue the families of invariant tori. Unlike for the families of periodic orbits, which are one-parameter families, invariant tori belong to two-parameter families [27]. Therefore, for consistency, it is necessary to fix one parameter within the family. Common choices include the rotation number and the Jacobi constant [27]. We compute the families of invariant tori at fixed Jacobi constants. Apart from this constraint, additional ones are necessary for the consistent continuation of the solutions. Note that if $\psi(\boldsymbol{\theta})$ is an invariant torus, $\psi(\boldsymbol{\theta}+\boldsymbol{\theta}_0)$, with $\boldsymbol{\theta}_0 \in \mathbb{R}^2$ would be a solution of the problem but not a different torus, i.e., the invariant curve would simply be phased in any of the two angles of the torus. Therefore, two phase constraints are included. Additionally, the pseudo-arclength constraint is used to ensure the next solution is at a certain distance from the previous one. In this study the tangent direction is obtained simply as the normalised difference between two already known solutions. For more details on these constraints,

the reader can consult Ref. [27].

The methodology described for computing families of quasi-periodic orbits is not the only approach available in the literature. Nevertheless, it has been shown that it is one of the most accurate and efficient methods [28].

3.3.2. Families of invariant tori in the vicinity of Earth

We start by studying quasi-periodic motion in the neighbourhood of the (displaced) L_1 point. Figure 7 showed that for all lightness numbers considered, the planar Lyapunov orbits around the (displaced) L_1 point have a centre manifold at the start of the families. Then, there is a pitchfork bifurcation, where the orbits stop being elliptic, giving rise to the halo families and the linear dynamics of the orbits become of type saddle×saddle [29]. Since invariant tori only exist around the planar orbits that have a central part, the planar Lyapunov orbits have quasi-periodic motion around them before they bifurcate into the halo family and later on when they regain their central part. Nevertheless, invariant tori still exist around both the vertical Lyapunov and halo orbits, see Fig. 10 and Fig. 13. In order to obtain the general picture, we compute the families of invariant tori around planar and vertical Lyapunov orbits as well as around halo orbits for $\beta = 0.02$ for different Jacobi values close to the bifurcation of the planar Lyapunov family into the halo family. For visualisation, the intersection of the families of tori with the ecliptic plane is plotted in Fig. 17, where the intersections for the planar and vertical Lyapunov as well as the halo orbits of the same Jacobi constant are represented in black and using black markers.

The figure shows that the quasi-periodic motion is bounded by the planar Lyapunov orbit. The quasi-periodic orbits around the planar and vertical Lyapunov orbits are referred to as Lissajous orbits, whereas the quasi-periodic ones around the halo orbits are referred to as quasi-halo orbits. For Jacobi constant values before the pitchfork bifurcation, the families of tori around the planar and vertical Lyapunov orbits are connected and all the quasi-periodic motion within the planar Lyapunov orbit presents the same structure. By connected it is meant that both families are actually the same and therefore it is possible to
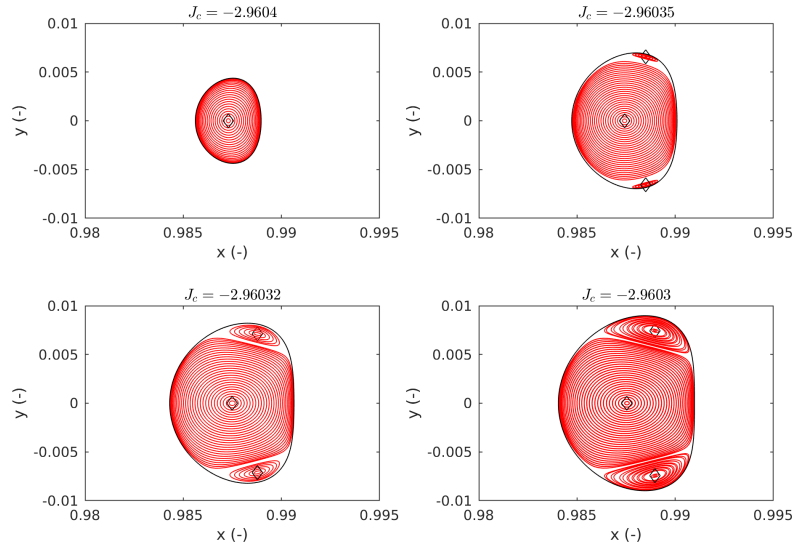
Figure 17: Intersections between Lissajous and quasi-halo families around SL_1 with the ecliptic plane for $\beta = 0.02$ at different Jacobi constants.

continue from a planar to a vertical Lyapunov orbit through a family of quasi-periodic orbits. Such connection was already shown for the CR3BP [26], but it persists when a solar-sail acceleration is included in the dynamics. When the Jacobi constant is increased, the planar Lyapunov orbits are no longer elliptic and no quasi-periodic motion exist around them until the orbits regain their central part. Furthermore, families of quasi-halos start to emerge, see top-right plot in Fig. 17, and they increase in size with increasing Jacobi constant. Figure 18 shows how the quasi-periodic orbits evolve throughout the Lissajous family around a vertical Lyapunov orbit around SL_1 for $\beta = 0.02$ and $J_c = -2.9604$. It is then clear how, first, the quasi-periodic orbits originate around the vertical Lyapunov orbit to later become a planar Lyapunov orbit.

The general picture for quasi-periodic motion around the (displaced) L_2 point is very similar to that around the (displaced) L_1 point. As it was shown in Fig. 7, the stability indices for the planar Lyapunov families around the (dis-

26
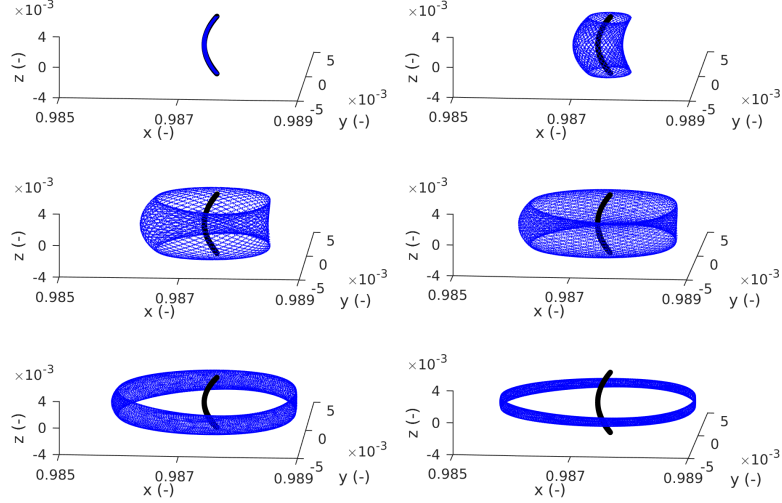
Figure 18: Evolution of the Lissajous quasi-periodic orbits around a vertical Lyapunov orbit around SL_1 for $\beta = 0.02$ and $J_c = -2.9604$.

placed) L_2 point generally behave like in the CR3BP for all lightness numbers considered. The orbits at the start of the planar Lyapunov families present a centre manifold, i.e., $s_2 = 2$. When the orbits grow in size, and increase their Jacobi constant, a bifurcation takes place where the orbits become hyperbolic and they lose their central part. Such point is where the families of halo orbits around the (displaced) L_2 point come into existence. The planar Lyapunov orbits then regain their central part when $s_2 = 2$. Regarding invariant tori around the vertical Lyapunov orbits around the (displaced) L_2 point, the vertical orbits have a centre manifold for a wide range of Jacobi constants as was shown in Fig. 10. Therefore, families of Lissajous orbits exist around such orbits. Lastly, for all lightness numbers, the halo orbits around the (displaced) L_2 have quasi-periodic motion around them, since, as Fig. 13 shows, $s_2 = 2$ for all orbits. Figure 19 depicts the intersection between the families of tori and the ecliptic around the SL_2 point for $\beta = 0.02$. Like for the quasi-periodic motion around

the SL_1 point, the families of invariant tori around vertical and planar Lyapunov orbits are connected when the Jacobi constant is smaller than the value at the bifurcation into the halo family. The connection between the families can be seen in the section in Fig. 19 for $J_c = -2.9612$, where all bounded motion within the planar Lyapunov orbit presents again the same structure. The planar family then bifurcates into the halo family and the planar orbits lose their centre manifold, breaking the connection with the Lissajous family around the vertical Lyapunov orbits. This is clear from the Poincaré sections for $J_c > -2.9612$. The quasi-halo families then start growing in size with the Jacobi constant. The evolution of the Lissajous families around the SL_2 point for $\beta = 0.02$ and $J_c = -2.9612$, where the families of tori around the planar and vertical Lyapunov orbits are connected, is shown in Fig. 20. It can be seen that the connection is very similar to the joined families around the SL_1 point shown in Fig. 18.
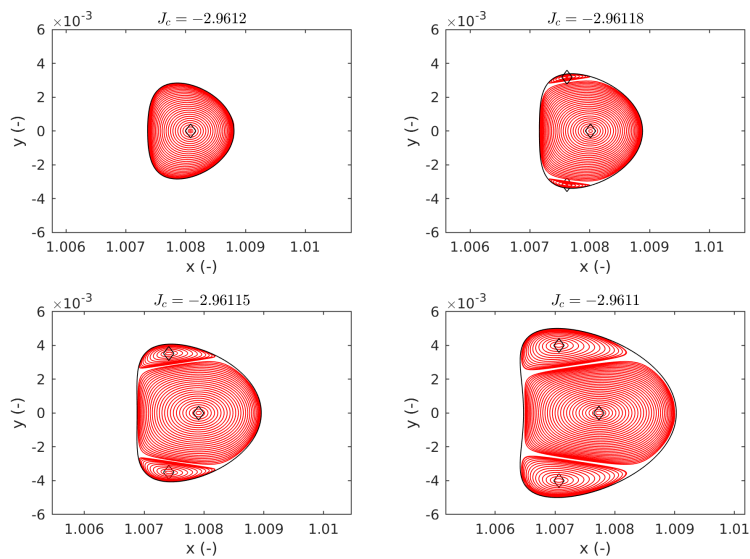
Figure 19: Intersections between Lissajous and quasi-halo families around SL_2 with the ecliptic plane for $\beta = 0.02$ at different Jacobi constants.

28
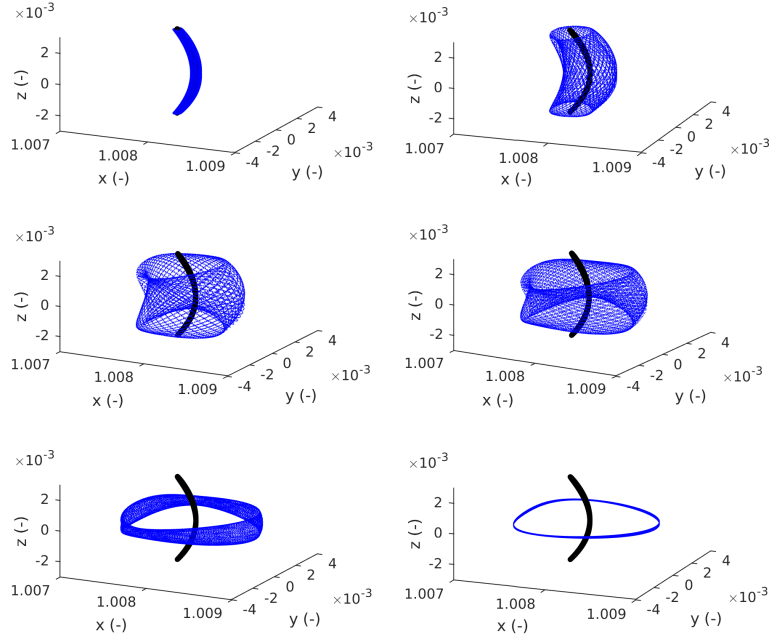
Figure 20: Evolution of the Lissajous quasi-periodic orbits around a vertical Lyapunov orbit around SL_2 for $\beta = 0.02$ and $J_c = -2.9612$.

It was shown that for the planar Lyapunov families around the (displaced) L_1 and L_2 points, the orbits regain their central part and families of invariant tori again start to exist around them. These orbits are no longer connected to the quasi-periodic orbits that exist around the vertical Lyapunov orbits that were shown in Figs. 18 and 20. Figure 21 depicts, around the SL_1 point, for $\beta = 0.02$ and $J_c = -2.96$ (see Fig. 7 (left) for $j_c = -0.9985$), quasi-periodic motion around planar and vertical Lyapunov and halo orbits. Similar results can be obtained around the (displaced) L_2 point.

3.3.3. Families of invariant tori in the L_5 region

Regarding the invariant tori that exist in the L_5 region, the linear dynamics around the planar and vertical Lyapunov orbits is of type centre×centre; there-

29
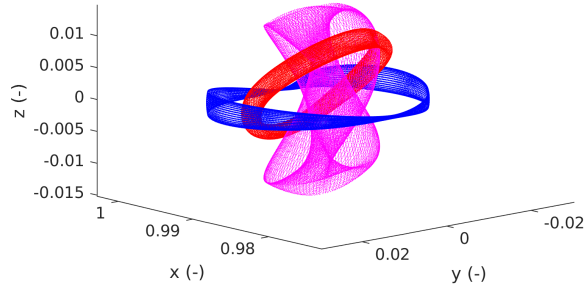
Figure 21: Examples of quasi-periodic orbits around a planar Lyapunov (blue) a vertical Lyapunov (magenta) and a halo (red) orbits around SL_1 for $\beta = 0.02$ and $J_c = -2.96$.

fore, it is possible to initiate the computation of invariant tori from such orbits with *two* initial guesses given by the two eigenvectors associated with the two eigenvalues within the unit circle. The initial guesses that can be constructed for invariant curves around the planar family result in two different families of invariant tori. However, for the quasi-periodic motion around the vertical orbits, both of the initial guesses that can be constructed result in the same family. As an example, we compute the families around a planar and a vertical Lyapunov orbits around the SL_5 point for $\beta = 0.02$ and Jacobi constant $J_c = -2.958$ and plot one member of each family in Fig. 22. The figure shows how for the quasi-periodic motion around planar orbits in the L_5 region, one of the families corresponds to in-plane quasi-periodic orbits (left) and the second family corresponds to out-of-plane quasi-periodic orbits (middle).

3.4. Invariant Manifolds

Equilibrium points, periodic orbits and quasi-periodic orbits can have different types of invariant manifolds which are very useful for mission design. This section describes how to compute them and justifies their importance.
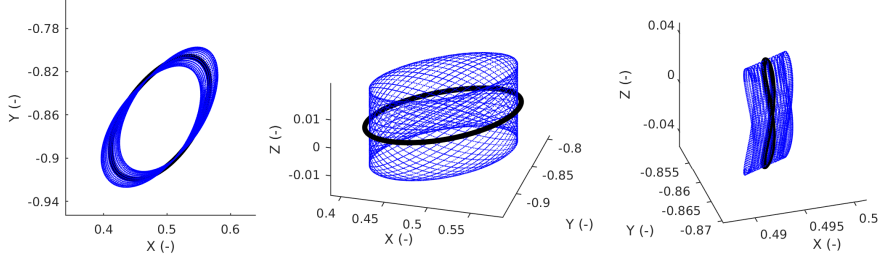
Figure 22: In-plane (left) and out-of-plane (middle) quasi-periodic orbits around a planar Lyapunov orbit and quasi-periodic orbit around a vertical Lyapunov orbit (right) around SL_5 for $\beta = 0.02$ and $J_c = -2.958$.

3.4.1. Invariant manifolds of equilibrium points

Let us assume $\boldsymbol{x}_e$ is a fixed (equilibrium) point of the non-linear system given by Eq. 8. Let us denote the matrix of the linearised system as Df. If Df has k eigenvalues with negative real part, j eigenvalues with positive real part and $m = 6 - k - j$ eigenvalues with zero real part, there exist a stable manifold W^s, an unstable manifold W^u and a centre manifold W^c; all of which are invariant under the flow. Such manifolds are tangent at $\boldsymbol{x}_e$ to the stable, unstable and centre subspaces given by the stable, unstable and centre directions of Df at $\boldsymbol{x}_e$. Furthermore, the stable and unstable manifolds are positively and negatively invariant respectively, satisfying [12]:

$$\lim_{t \to \infty} \phi_t(\boldsymbol{v}, \alpha, \delta) = \boldsymbol{x}_e \quad \text{for all} \quad \boldsymbol{v} \in W^s, \tag{28}$$

$$\lim_{t \to -\infty} \phi_t(\boldsymbol{v}, \alpha, \delta) = \boldsymbol{x}_e \quad \text{for all} \quad \boldsymbol{v} \in W^u. \tag{29}$$

Numerically, the stable and unstable manifolds associated with the equilibrium point $\boldsymbol{x}_e$ can be computed as

$$W^s = \{\boldsymbol{x} : \phi_t(\boldsymbol{x}_e \pm \epsilon \boldsymbol{u}_s, \alpha, \delta) - \boldsymbol{x} = 0 \quad \text{for} \quad t \in \mathbb{R}_{\leq 0}\}, \tag{30}$$

$$W^u = \{\boldsymbol{x} : \phi_t(\boldsymbol{x}_e \pm \epsilon \boldsymbol{u}_u, \alpha, \delta) - \boldsymbol{x} = 0 \quad \text{for} \quad t \in \mathbb{R}_{\geq 0}\}, \tag{31}$$

where ϵ is the magnitude of the perturbation, taken as 10^{-5}, $\boldsymbol{u}_s$ is the unit eigenvector of Df associated with the stable direction and $\boldsymbol{u}_u$ is the unit eigenvector of Df associated with the unstable direction [30]. The relevance of these

topological spaces for mission design is clear as a spacecraft travelling along the stable manifold of an equilibrium point will eventually reach it, whereas along the unstable manifold, the spacecraft will divert from the equilibrium point.

Figure 23 depicts the stable and unstable manifolds of the collinear equilibrium points for $\beta \in \{0, 0.01, ..., 0.05\}$. For the analysis in §4 it is important to note that, as the figure shows, it is not possible to reach the L_5 region along the unstable manifold from the natural L_1 point ($\beta = 0$). Furthermore, for $\beta = 0.01$, a transfer along the unstable manifold associated with the SL_1 point gets entangled around Earth before escaping towards the L_5 region [7]. These cases will therefore require additional considerations for the mission design that will be discussed later on.
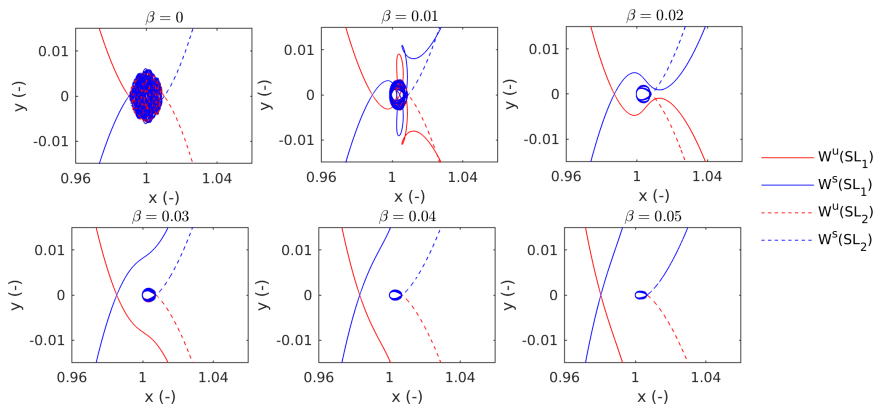
Figure 23: Stable and unstable manifolds of the (displaced) L_1 and L_2 points for $\beta \in \{0, 0.01, ..., 0.05\}$.

3.4.2. Invariant manifolds of periodic orbits

Regarding the invariant manifolds of periodic orbits, let us first assume $\boldsymbol{x}_p$ defines a periodic orbit with period T and sail attitude α and δ. We can define the cycle of a periodic orbit as the set

$$\Gamma = \{\boldsymbol{x} : \phi_t(\boldsymbol{x}_p, \alpha, \delta) - \boldsymbol{x} = 0 \quad \text{for} \quad t \in [0, T)\}. \tag{32}$$

If k of the eigenvalues of the monodromy matrix of Γ are outside the unit circle centred at the origin of $\mathbb{C}$, j are inside and $m = 6 - k - j$ are on the

boundary, there exist a stable manifold W^s, an unstable manifold W^u and a centre manifold W^c; all invariant under the flow. Furthermore, the stable manifold W^s, the unstable manifold W^u and the centre manifold W^c intersect transversally in Γ. Additionally, the stable and unstable manifolds are positively and negatively invariant under the flow and satisfy [12]:

$$\lim_{t \to \infty} \phi_t(\boldsymbol{v}, \alpha, \delta) \in \Gamma \quad \text{for all} \quad \boldsymbol{v} \in W^s \tag{33}$$

$$\lim_{t \to -\infty} \phi_t(\boldsymbol{v}, \alpha, \delta) \in \Gamma \quad \text{for all} \quad \boldsymbol{v} \in W^u. \tag{34}$$

Numerically, the stable and unstable manifolds associated with the periodic orbit can be computed as [30]

$$W^s = \{\boldsymbol{x} : \phi_t(\boldsymbol{z} \pm \epsilon \boldsymbol{y}_s(\boldsymbol{z}), \alpha, \delta) - \boldsymbol{x} = 0 \quad \text{for} \quad \boldsymbol{z} \in \Gamma, t \in \mathbb{R}_{\leq 0}\}, \tag{35}$$

$$W^u = \{\boldsymbol{x} : \phi_t(\boldsymbol{z} \pm \epsilon \boldsymbol{y}_u(\boldsymbol{z}), \alpha, \delta) - \boldsymbol{x} = 0 \quad \text{for} \quad \boldsymbol{z} \in \Gamma, t \in \mathbb{R}_{\geq 0}\}, \tag{36}$$

where $\boldsymbol{y}_s(\boldsymbol{z})$ and $\boldsymbol{y}_u(\boldsymbol{z})$ are the stable and unstable eigenvectors at $\boldsymbol{z} \in \Gamma$. If $\boldsymbol{y}_i$, with $i = s, u$, are eigenvectors of the monodromy matrix at $\boldsymbol{x}_p$, they can be translated anywhere along Γ as $\boldsymbol{y}_i(\boldsymbol{z}) = \Phi(t, \boldsymbol{x}_p, \alpha, \delta)\boldsymbol{y}_i$, where $\boldsymbol{z} = \phi_t(\boldsymbol{x}_p, \alpha, \delta)$ [30]. As an example, Fig. 24 shows the stable and unstable manifolds of a solar-sail halo orbit around the displaced L_1 point for $\beta = 0.02$. The figure shows that a spacecraft could escape Earth along the unstable manifold of the halo orbit; therefore, the invariant manifolds of periodic orbits can once again be very useful for mission design, see §4.
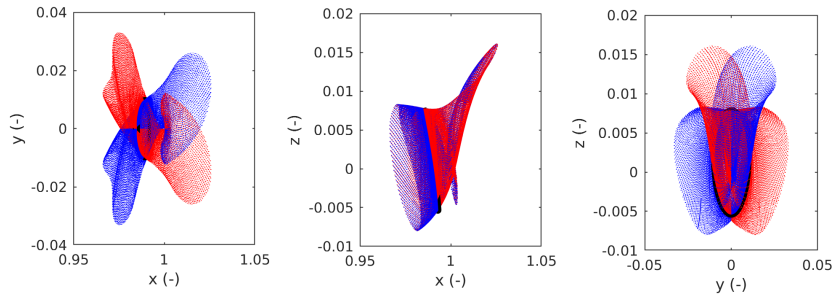
Figure 24: Stable (blue) and unstable (red) manifolds of a halo orbit around SL_1 for $\beta = 0.02$.

3.4.3. Invariant manifolds of quasi-periodic orbits

A matrix analogous to the monodromy matrix exists for quasi-periodic orbits from which stability information and the associated invariant manifolds can be obtained. We follow Ref. [27] and asses the stability of a quasi-periodic orbit through the variation of the rotated mapped invariant curve under the stroboscopic map with respect to the invariant curve, i.e.,

$$\frac{d}{d\varphi}\left(R(-\rho) \circ \phi_{T_2}(\varphi(\xi), \alpha, \delta)\right). \tag{37}$$

Such a matrix appears in the computation of quasi-periodic orbits. The computation of their associated invariant manifolds therefore requires little extra effort. The matrix in Eq. 37 is nothing else than the linearisation of the stroboscopic map, but removing the rotation to asses the stability of the curve $\varphi(\xi)$ as opposed to that of the mapped curve $\varphi(\xi + \rho)$ [27]. The eigenvectors associated with the real eigenvalues of the stability matrix then correspond to the stable and unstable directions of the invariant manifolds at each point of the discretised invariant curve at some reference value for the angular coordinate $\theta_2 = \theta_2^0$ [27]. In order to compute the invariant manifolds anywhere on the torus, i.e., $\theta_2 = \theta_2^0 + \omega_2 t$, the eigenvectors of the stability matrix at the invariant curve need to be translated along θ_2. Let us assume $\boldsymbol{Y}$ is the (un)stable eigenvector of $\varphi(\xi)$ at $\theta_2 = \theta_2^0$. Then, the (un)stable directions along the torus $\boldsymbol{Y}(\theta_2)$ are given by [27]

$$\boldsymbol{Y}(\theta_2) = \Phi(\varphi(\xi), t, \alpha, \delta))\boldsymbol{Y}. \tag{38}$$

As an example, Fig. 25 shows the stable and unstable directions of a quasi-halo orbit around the displaced L_2 point for $\beta = 0.02$.

4. Trajectory design between invariant objects

In this study, we consider transfers between the collinear equilibrium points in the vicinity of Earth and families of periodic orbits in the L_5 region, transfers between families of periodic orbits and transfers between families of quasi-periodic orbits. In order to find these transfers, we first use a multi-objective
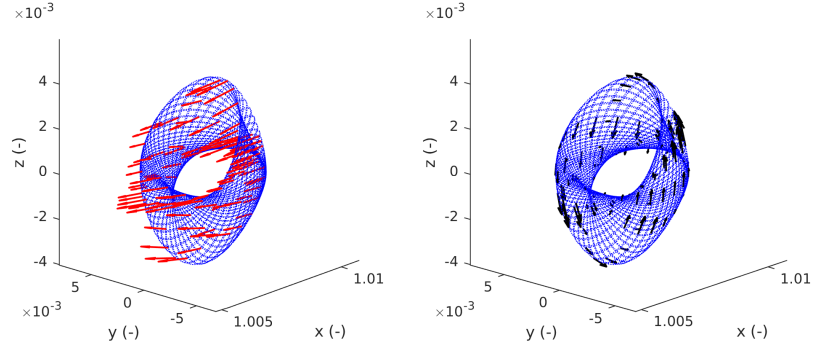
Figure 25: Stable (black) and unstable (red) directions along a quasi-halo orbit around the SL_2 point for $\beta = 0.02$.

genetic algorithm to find initial guesses that are refined and optimised with a multiple-shooting differential corrector and a continuation of the solutions with the time of flight. Finally, the optimality of the transfers is checked by comparing the results with those obtained with the optimal control solver PSOPT.

4.1. Genetic algorithm

A genetic algorithm (implemented using the MATLAB® function *gamultiobj.m*) is taken at hand to solve a multi-objective optimisation problem in which a set of decision variables defines a guess for the transfer. The quality of that guess is assessed in terms of the two objectives: the infeasibility, ϵ_I, and the time of flight (TOF). Since the decision variables vary for each case, i.e., the type of invariant objects used for the departure and arrival conditions, each case will be discussed separately below.

4.1.1. Transfers between the collinear equilibrium points and families of periodic orbits in the L_5 region

The initial guesses are obtained as the union of two segments: one starting at the collinear equilibrium point and another one coming from the L_5 region. The unstable manifolds originating from the displaced equilibrium points are

35

used for the first segment and they are integrated over a five year time frame, forwards in time. However, note that the unstable manifold of the L_1 and L_2 points enters a complex region around Earth as was shown in Fig. 23. This can cause issues in the adopted approach. Therefore, in those cases, we use manifold-like trajectories that start from the L_1 and L_2 points perturbed in the direction of the unstable manifold but including a solar-sail acceleration where the solar sail is pitched at a fixed, zero degree angle with respect to the incoming solar radiation. Figure 26 depicts these stable and unstable manifold-like trajectories $\tilde{W}^s$ and $\tilde{W}^u$ departing from L_1 and L_2. The figure shows that for $\beta = 0.01$ the unstable manifold-like trajectory loops around Earth but still manages to escape from it. For $\beta > 0.01$, the solar sail successfully escapes without revolving around Earth. Note that for $\beta = 0$, the manifold and the manifold-like trajectories are the same as no solar-sail acceleration is included; therefore, the trajectories still enter the complex region around Earth.
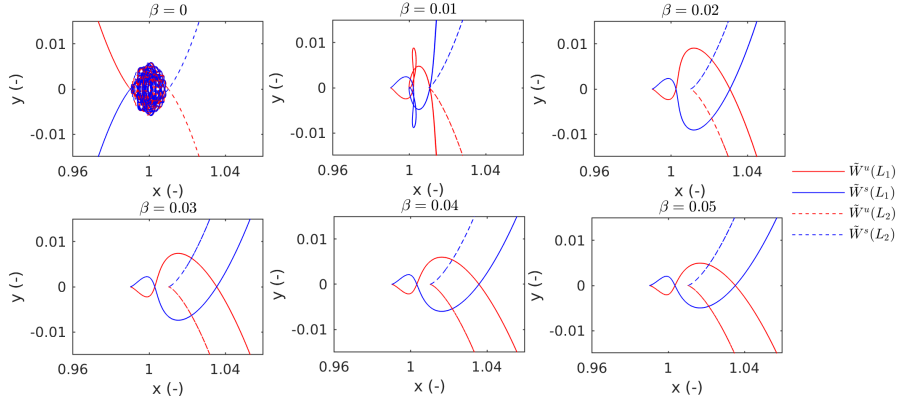
Figure 26: Stable and unstable manifolds-like trajectories of the L_1 and L_2 points for $\beta \in \{0, 0.01, ..., 0.05\}$.

The target periodic orbit, insertion conditions and the segment reaching the L_5 region are determined with a vector of decision variables, $\mathbf{x}$, defined as:

$$\mathbf{x} = [d_f \quad \tau_f \quad \alpha_f]. \tag{39}$$

Given a family of periodic orbits around the (displaced) L_5 point, the first vari-

able, d_f, determines the dimensionless size of the periodic orbit as the largest distance from the periodic orbit to its associated equilibrium point. This variable allows transfers that target entire families of periodic orbits, as opposed to works that target one particular periodic orbit [4, 6]. The second variable, τ_f, determines the insertion point into the periodic orbit. Such a point is obtained from propagating the flow over a time $\tau_f T$, where T is the periodic orbit period, starting from some reference point. Finally, the third variable, α_f, determines the constant cone angle of the sail which is used in the backwards integration from the insertion point over a five year time frame. Figure 27 depicts how the vector of decision variables defines the target periodic orbit around the (displaced) L_5 point, the insertion point and the segment of the trajectory reaching the L_5 region. Note that since this is a planar problem, $\delta = \pi/2$.
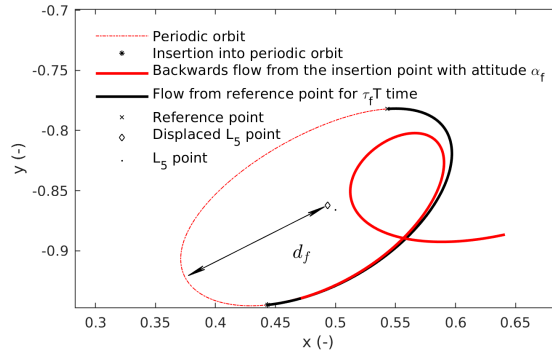
Figure 27: Schematic of genetic algorithm decision variables.

The initial guess for the transfer is then given by the union of the unstable manifold or the unstable manifold-like trajectory of the equilibrium point and the backwards flow from the periodic orbit at the point of minimum Euclidean norm in dimensionless phase space. This value is used as the infeasibility objective, ϵ_I. Together with the corresponding time of flight, the genetic algorithm creates a Pareto front that gives a range of potential initial guesses that vary in feasibility and time of flight. Ideally, the initial guess selected for the next steps of the trajectory design is the guess which is sufficiently feasible and has the

smallest time of flight, where, by sufficiently feasible, it is meant that the initial guess can converge to a feasible solution with the multiple shooting differential corrector approach, see §4.2.

As an example, Fig. 28 (left) shows the Pareto front obtained for transfers from the natural L_1 point to the solar-sail planar Lyapunov family around the SL_5 point for $\beta = 0.02$. An initial guess, highlighted in red in the Pareto front, is depicted in Fig. 28 (right). In terms of objective values, this initial guess achieves a feasibility of $\epsilon_I = 0.0344$, which corresponds to an error in position of $2.15 \cdot 10^6$ km and an error in synodic velocity of 0.9292 km/s. The time of flight equals TOF $= 738$ days, while the values for the decision variables are: $\mathbf{x} = [d_f \quad \tau_f \quad \alpha_f] = [0.1858 \quad 0.3227 \quad 28.89]$, where α_f is given in degrees.
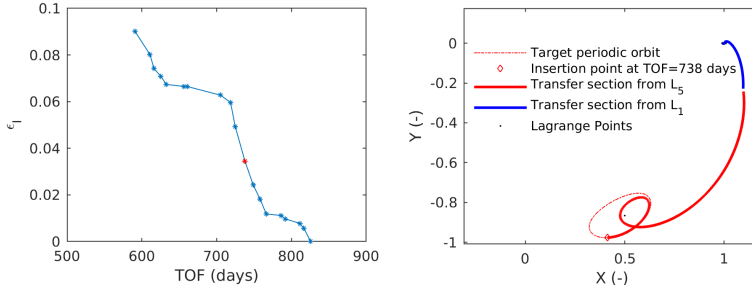
Figure 28: Examples of the Pareto front obtained with the genetic algorithm (left) and of an initial guess (right) for transfers from the natural L_1 point to the solar-sail planar Lyapunov family around the SL_5 point for $\beta = 0.02$.

4.1.2. Transfers between families of periodic orbits

When the departure invariant object is a periodic orbit within an orbit family around the L_1, L_2, SL_1 or SL_2 points, the decision vector in Eq. 39 is expanded to:

$$\mathbf{x} = [d_0 \quad \tau_0 \quad d_f \quad \tau_f \quad \alpha_f \quad \delta_f]. \tag{40}$$

Equation 40 now also includes decision variables to select the best size of the departing orbit, d_0, and the best departure condition along that orbit, τ_0. Furthermore, if the departing periodic orbit is a three-dimensional orbit, the angle

δ_f considers a solar-sail attitude component in the out-of-plane direction in the backwards propagation from the L_5 region.

Similar to the approach in §4.1.1, the departure conditions are propagated along the unstable manifold, only now of the periodic orbit, for a five year time frame. The initial guess is then again obtained as the union of the trajectory along the unstable manifold of the periodic orbit and the backwards flow from the periodic orbit around L_5 or SL_5 at the point of minimum Euclidean norm in dimensionless phase space.

The unstable manifolds of the natural periodic orbits around L_1 and L_2 do not present the complex region around Earth that the manifolds associated with the natural collinear equilibrium points do. Nevertheless, the initial guesses benefit, in terms of TOF, from using the sail at a zero degree angle with respect to the incoming solar flux. Therefore, the approach described for the unstable manifolds of the collinear Lagrange points is also adopted for the unstable manifolds of natural periodic orbits. When departing from solar-sail periodic orbits, their associated unstable manifolds already have a sail attitude aligned with the incoming flux. Therefore the true unstable manifolds are used.

4.1.3. Transfers between families of quasi-periodic orbits

In order to explore trajectories between families of quasi-periodic orbits, we use three new variables. The first is a variable that determines the invariant curve that defines the quasi-periodic orbit for the arrival or departure conditions, see Fig. 29 (left) for the initial conditions. This variable is defined as the maximum distance from the invariant curve to the periodic orbit and denoted by ϱ_i with $i = 0, f$, where the subscript 0 denotes departure and the subscript f denotes arrival conditions. Note that the point of the periodic orbit used to define this variable is the point of the periodic orbit from where the invariant curves originate. To determine the position within the quasi-periodic orbit where the spacecraft departs or arrives, two variables are needed as invariant tori are 2-dimensional surfaces. Therefore, the second new variable is θ_{1i}, with $i = 0, f$, that parameterises the invariant curve, defining the point $\psi(\boldsymbol{\theta})$, with

$\boldsymbol{\theta} = [\theta_{1i} \quad \theta_{2i}]^T$, where θ_{2i} is the reference value for the angular variable θ_2 of the torus where the invariant curve is located, see Fig. 29. The third parameter, ζ_i, allows to explore the torus in the variable θ_2 by propagating the point from the invariant curve defined by ϱ_i and θ_{1i} for a time $\zeta_i T_{2i}$, where T_{2i} is the period associated with the motion in θ_2 within the departure or arrival quasi-periodic orbit.
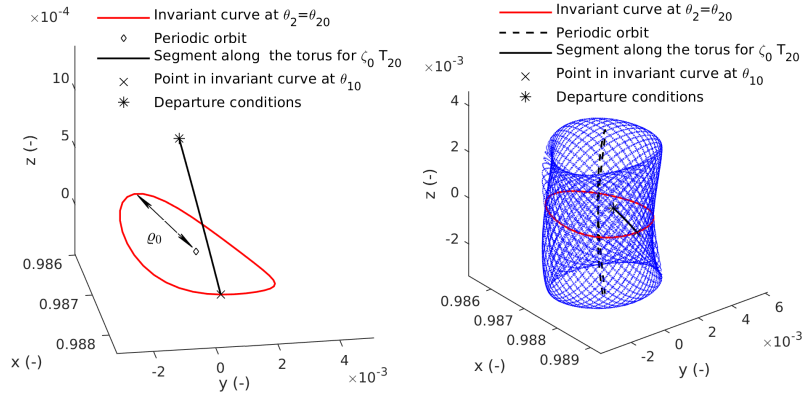
Figure 29: Initial conditions for departure from a natural Lissajous orbit around L_1 on the invariant curve (left) and on the quasi-periodic orbit (right).

The defined variables fully determine the departing and arriving conditions in the quasi-periodic orbits. Such conditions can be mathematically expressed as

$$\phi_{\zeta_0 T_{20}}(\varphi_0(\theta_{10}), \alpha, \delta), \tag{41}$$

$$\phi_{\zeta_f T_{2f}}(\varphi_f(\theta_{1f}), \alpha, \delta), \tag{42}$$

where, φ_0 and φ_f are the invariant curves for the departure and arrival quasi-periodic orbits. The initial guess can then be obtained, similarly as for the cases in §4.1.1 and §4.1.2, as the union of two segments coming from the departure and arrival quasi-periodic orbits. The departing quasi-periodic orbits around the (displaced) L_1 and L_2 points have unstable manifolds; therefore, for the first segment of the transfer, the departure conditions are propagated along the unstable manifold of the quasi-periodic orbit for a five year time frame. In order

for the initial guesses, departing from natural quasi-periodic orbits, to benefit from the sail, the same manifolds-like trajectories previously described are used. The quasi-periodic orbits in the L_5 region are stable and therefore the second segment is obtained as the backwards flow from the arrival conditions with some sail attitude given by the variables α_f and δ_f. The initial guess is then defined by

$$\mathbf{x} = [\varrho_0 \quad \theta_{10} \quad \zeta_0 \quad \varrho_f \quad \theta_{1f} \quad \zeta_f \quad \alpha_f \quad \delta_f]. \tag{43}$$

4.2. Multiple shooting differential corrector

The transfers obtained with the genetic algorithm will not be feasible nor time-optimal. We therefore use a multiple shooting differential corrector to first turn the genetic algorithm guesses into feasible trajectories and then reduce the time of flight.

First, the guesses are discretised on $n = 30$ nodes. The decision vector at each node contains a point in phase space, a cone angle, a clock angle and a temporal variable. They can be expressed as:

$$\boldsymbol{X}_i = \begin{bmatrix} \boldsymbol{x}_i \\ \alpha_i \\ \delta_i \\ t_i \end{bmatrix} \quad \text{for} \quad i \in \{1, 2, ...n\} \tag{44}$$

A feasible trajectory for a given TOF, T_0, with constraints g_0 and g_f on the initial and final nodes is obtained as the solution to the following problem:

$$g_0(\boldsymbol{X}_1) = 0 \tag{45}$$

$$\phi_{t_i}(\boldsymbol{x}_i, \alpha_i, \delta_i) - \boldsymbol{x}_{i+1} = 0 \quad \text{for} \quad i \in \{1, 2, ..., n-1\} \tag{46}$$

$$g_f(\boldsymbol{X}_n) = 0 \tag{47}$$

$$\sum_{i=1}^{n-1} t_i - T_0 = 0 \tag{48}$$

The constraints g_0 and g_f depend on the departure and arrival conditions selected. We can rewrite Eqs. 45-48 as $S(\boldsymbol{X}) = 0$, with $\boldsymbol{X} = [\boldsymbol{X}_1^T, \boldsymbol{X}_2^T, ...\boldsymbol{X}_n^T]^T$.

Then, an initial guess $\hat{\boldsymbol{X}}$ can be corrected by solving the linear system:

$$-S(\hat{\boldsymbol{X}}) = JS(\hat{\boldsymbol{X}})\delta\boldsymbol{X}, \qquad (49)$$

where $JS(\boldsymbol{X}) =$

$$\begin{bmatrix} Jg_0(\boldsymbol{X}_1) & 0 & \cdots & \cdots & \cdots & \cdots & 0 \\ \tilde{\Phi}_1 & f_1 & -E & 0 & \cdots & \cdots & 0 \\ 0 & \tilde{\Phi}_2 & f_2 & -E & 0 & \cdots & 0 \\ \vdots & \ddots & \ddots & \ddots & \ddots & \ddots & \vdots \\ 0 & \cdots & \cdots & \tilde{\Phi}_{n-2} & f_{n-2} & -E & 0 \\ 0 & \cdots & \cdots & \cdots & \tilde{\Phi}_{n-1} & f_{n-1} & -E \\ 0 & \cdots & \cdots & \cdots & \cdots & \cdots & Jg_f(\boldsymbol{X_n}) \\ u & \cdots & \cdots & \cdots & \cdots & u & 0 \end{bmatrix}, \qquad (50)$$

where $f_i = f(\phi_{t_i}(\boldsymbol{x}_i, \alpha_i, \delta_i), \alpha_i, \delta_i)$ with $i \in \{1, 2, ..., n-1\}$, $E = [I_{6\times6} \quad 0_{6\times3}]$, $u = [0_{1\times8} \quad 1]$ and $\tilde{\Phi}_i = \tilde{\Phi}(\boldsymbol{x}_i, t_i, \alpha_i, \delta_i)$ with $i \in \{1, 2, ..., n-1\}$. The 6×8 matrix $\tilde{\Phi}$ is an expanded STM that includes the variation of $\phi_{t_i}(\boldsymbol{x}_i, \alpha_i, \delta_i)$ with respect to α_i and δ_i, i.e., $\tilde{\Phi} = [\Phi \quad \frac{\partial\phi_t}{\partial\alpha} \quad \frac{\partial\phi_t}{\partial\delta}]$ [6].

For some cases, the decision vectors for the initial and/or final node, as they appear in Eq. 44, need to be changed in order to impose the boundary constraints on them. Then, due to the addition or elimination of variables for the outer nodes the Jacobian of $S(\boldsymbol{X})$, as it appears in Eq. 50, needs to be slightly modified to account for the variables used. Nevertheless, the general structure of $JS(\boldsymbol{X})$ is maintained.

4.2.1. Transfers between the collinear equilibrium points and families of periodic orbits in the L_5 region

This case is equivalent to fixing $\boldsymbol{x}_1$ to the desired departure collinear equilibrium point, $\boldsymbol{x}_{fixed}$, and imposing the constraint given by Eq. 11 to $\boldsymbol{X}_n$. The decision vector for the first node can then be expressed as in Eq. 44, whereas for the last node it is defined only by point in phase space and the period of the

orbit it belongs to, T_n. Therefore,

$$\boldsymbol{X}_1 = \begin{bmatrix} \boldsymbol{x}_1 \\ \alpha_1 \\ \delta_1 \\ t_1 \end{bmatrix}, \quad \boldsymbol{X}_n = \begin{bmatrix} \boldsymbol{x}_n \\ T_n \end{bmatrix}. \tag{51}$$

The constraints on the outer nodes are then defined as:

$$g_0(\boldsymbol{X}_1) = \boldsymbol{x}_1 - \boldsymbol{x}_{fixed}, \tag{52}$$

$$g_f(\boldsymbol{X}_n) = G(\boldsymbol{x}_n, T_n) = \phi_{T_n}(\boldsymbol{x}_n, \alpha, \delta) - \boldsymbol{x}_n. \tag{53}$$

If $\boldsymbol{X}_n$ defines a periodic orbit from an specific family, the constraint given by Eq. 53 will generally set the last node to an orbit belonging to that family, unless the periodic orbit of the initial guess is close to a bifurcation point.

4.2.2. Transfers between families of periodic orbits

If the initial point, $\boldsymbol{x}_1$, is constrained to be on a family of periodic orbits, the variables for the initial node, $\boldsymbol{X}_1$, as they appear in Eq. 44, are not sufficient to define a departure periodic orbit. It would be possible to expand $\boldsymbol{X}_1$ with an extra variable, T_1, to define the period of the departure periodic orbit and impose Eq. 11 to the initial node in a similar way as was done for the last node in Eq. 53. However, this does not work well in practice because the departing periodic orbits are unstable for which the differential corrector has difficulties converging to fast transfers. Therefore, in order to be able to let the initial node belong to a family of unstable periodic orbits around the collinear equilibrium points, a more robust periodicity constraint is explored.

Let us consider a set defined by a point $\boldsymbol{x}_p$, a parameter T and fixed cone and clock angles α and δ respectively. The complete set can be expressed as

$$\Gamma = \{\boldsymbol{x} : \phi_t(\boldsymbol{x}_p, \alpha, \delta) - \boldsymbol{x} = 0 \quad \text{for} \quad t \in [0, T)\}. \tag{54}$$

Then, the set Γ defines a periodic orbit if for any $\boldsymbol{x} \in \Gamma$, $G(\boldsymbol{x}, T) = 0$. This can be expressed as:

$$\tilde{G}(\boldsymbol{x}, T, t) = \phi_T(\phi_t(\boldsymbol{x}, \alpha, \delta), \alpha, \delta) - \phi_t(\boldsymbol{x}, \alpha, \delta) = 0, \tag{55}$$

with $t \in [0, T)$. Equation 55 is a more robust periodicity constraint as it allows to impose periodicity not at $\boldsymbol{x}$ but at $\phi_t(\boldsymbol{x}, \alpha, \delta)$. By the theorem of existence and uniqueness of differential equations [12], if $\phi_t(\boldsymbol{x}, \alpha, \delta)$ belongs to a periodic orbit, so will $\boldsymbol{x}$. Note, that $\tilde{G}$ can also be used to compute exclusively periodic orbits.

For this case, the decision vectors for the initial and final nodes are expressed as:

$$
\boldsymbol{X}_1 = \begin{bmatrix} \boldsymbol{x}_1 \\ \alpha_1 \\ \delta_1 \\ t_1 \\ T_1 \\ \tilde{t}_1 \end{bmatrix}, \quad \boldsymbol{X}_n = \begin{bmatrix} \boldsymbol{x}_n \\ T_n \\ \tilde{t}_n \end{bmatrix}, \tag{56}
$$

where $\tilde{t}_1$ and $\tilde{t}_n$ are used for the variable t in $\tilde{G}$ in Eq. 55. The constraints on the initial and final node are then:

$$
g_0(\boldsymbol{X}_1) = \tilde{G}(\boldsymbol{x}_1, T_1, \tilde{t}_1) = \phi_{T_1}(\phi_{\tilde{t}_1}(\boldsymbol{x}_1, \alpha, \delta), \alpha, \delta) - \phi_{\tilde{t}_1}(\boldsymbol{x}_1, \alpha, \delta), \tag{57}
$$

$$
g_f(\boldsymbol{X}_n) = \tilde{G}(\boldsymbol{x}_n, T_n, \tilde{t}_n) = \phi_{T_n}(\phi_{\tilde{t}_n}(\boldsymbol{x}_n, \alpha, \delta), \alpha, \delta) - \phi_{\tilde{t}_n}(\boldsymbol{x}_n, \alpha, \delta). \tag{58}
$$

To include the new periodicity constraints, the Jacobian of $\tilde{G}$ is needed for inclusion in Eq. 50 and can be expressed as:

$$
\begin{aligned}
J\tilde{G} &= [\frac{\partial \tilde{G}}{\partial \boldsymbol{x}} \quad \frac{\partial \tilde{G}}{\partial T} \quad \frac{\partial \tilde{G}}{\partial t}] \\
&= [(\Phi(\phi_t(\boldsymbol{x}, \alpha, \delta), T, \alpha, \delta) - I_{6 \times 6})\Phi(\boldsymbol{x}, t, \alpha, \delta) \quad f(\phi_T(\phi_t(\boldsymbol{x}, \alpha, \delta), \alpha, \delta)) \\
&\quad (\Phi(\phi_t(\boldsymbol{x}, \alpha, \delta), T, \alpha, \delta) - I_{6 \times 6})f(\phi_t(\boldsymbol{x}, \alpha, \delta), \alpha, \delta)].
\end{aligned}
\tag{59}
$$

Note that both the constraints in Eq. 11 and 55 can be used to constrain a node to a family of periodic orbits. However, it might be of interest to actually fix the departure and/or arrival orbits in the scenario where the mission requirements constrain the departure and/or arrival orbits. Then, let us assume we want to fix a point $\boldsymbol{x}$ to lie on a specific periodic orbit. Such a periodic orbit

can be described by a phase space point $\boldsymbol{x}_p$, a period T and cone and clock angles α and δ. Then the point $\boldsymbol{x}$ needs to satisfy:

$$\mathring{G}(\boldsymbol{x}, t) = \phi_t(\boldsymbol{x}_p, \alpha, \delta) - \boldsymbol{x} = 0, \tag{60}$$

for some $t \in [0, T)$. Lastly, the Jacobian of $\mathring{G}$ needed for inclusion in Eq. 50 can be obtained as:

$$J\mathring{G} = [-I_{6\times6} \quad f(\phi_t(\boldsymbol{x}_p, \alpha, \delta), \alpha, \delta)]. \tag{61}$$

4.2.3. Transfers between quasi-periodic orbits

Let us assume we want to depart from a quasi-periodic orbit defined by the invariant curve $\varphi_0(\xi)$. Let us also assume we would like to arrive to a quasi-periodic orbit in the L_5 region defined by the invariant curve $\varphi_f(\xi)$. The genetic algorithm will obtain the departure and arrival quasi-periodic orbits at the conditions expressed in Eqs. 41 and 42. Then, we can constrain the initial and final nodes of the transfers to be within the selected quasi-periodic orbits by rotating the conditions $\varphi_i(\theta_{1i})$ with $i = 0, f$ by some rotation number $\delta\rho_i$ and propagate the flow from such conditions along the quasi-periodic orbit for some time $\zeta_i T_{2i}$. The constraint to fix a node to quasi-periodic orbits can then be expressed as

$$\bar{G}(\boldsymbol{x}, \delta\rho, \zeta) = \phi_{\zeta T_2}(R(\delta\rho) \circ \varphi(\xi_{ref}), \alpha, \delta) - \boldsymbol{x} = 0, \tag{62}$$

where R is the rotation operator defined in §3.3 that rotates points within invariant curves and ξ_{ref} defines a reference point in the invariant curve taken as $\xi_{ref} = \theta_{10}$ for the departure torus and as $\xi_{ref} = \theta_{1f}$ for the arrival one.

To impose the quasi-periodic orbit constraint to the outer nodes it is necessary to include the parameters $\delta\rho_i$ and ζ_i to the decision vectors which can

then be expressed as

$$\boldsymbol{X}_1 = \begin{bmatrix} \boldsymbol{x}_1 \\ \alpha_1 \\ \delta_1 \\ \delta\rho_0 \\ \zeta_0 \end{bmatrix}, \quad \boldsymbol{X}_n = \begin{bmatrix} \boldsymbol{x}_n \\ \delta\rho_f \\ \zeta_f \end{bmatrix}. \tag{63}$$

The constraints on the initial and final nodes then become

$$g_0(\boldsymbol{X}_1) = \bar{G}(\boldsymbol{x}_1, \delta\rho_0, \zeta_0) = \phi_{\zeta_0 T_{20}}(R(\delta\rho_0) \circ \varphi(\theta_0), \alpha, \delta) - \boldsymbol{x}_1, \tag{64}$$

$$g_f(\boldsymbol{X}_n) = \bar{G}(\boldsymbol{x}_n, \delta\rho_f, \zeta_f) = \phi_{\zeta_f T_{2f}}(R(\delta\rho_f) \circ \varphi(\theta_f), \alpha, \delta) - \boldsymbol{x}_n. \tag{65}$$

Lastly, the Jacobian of Eq. 62 can be computed as

$$\begin{aligned} J\bar{G} &= [\frac{\partial \bar{G}}{\partial \boldsymbol{x}} \quad \frac{\partial \bar{G}}{\partial \delta\rho} \quad \frac{\partial \bar{G}}{\partial \zeta}] \\ &= [-I_{6\times 6} \quad \Phi(R(\delta\rho) \circ \varphi(\xi_{ref}), \zeta T_2, \alpha, \delta)\frac{dR(\delta\rho)}{d\delta\rho} \circ \varphi(\xi_{ref}) \\ & \quad\quad f(\phi_{\zeta T_2}(R(\delta\rho) \circ \varphi(\xi_{ref}), \alpha, \delta), \alpha, \delta)]. \end{aligned} \tag{66}$$

4.3. Optimisation with the multiple shooting differential corrector

So far, the differential corrector described computes transfers for a fixed TOF: the initial guess given by the genetic algorithm is used to seed the differential corrector and find a feasible trajectory with the TOF, T_0, of the initial guess. To optimise the transfer with respect to the time of flight, this solution is then used to compute a new solution for a time of flight κT_0, with $\kappa < 1$. This process is iterated until the differential corrector does not converge. Then, the factor κ is increased to allow smaller steps in the continuation. We use $\kappa \in \{0.95, 0.98, 0.99, 0.999, 0.9995\}$.

4.4. Additional case

The cases described for both the genetic algorithm and the multiple shooting differential corrector can be combined and slightly modified to build new cases without much difficulty. For instance, we consider the case where a primary

mission is launched into the stable manifold of a natural halo orbit around the L_1 point. At some point along the stable manifold, a secondary spacecraft equipped with a solar sail is separated from the primary spacecraft to begin its trajectory to the planar Lyapunov family around the L_5 point. We are interested in finding and optimising a trajectory departing from the stable manifold of a particular halo orbit and arriving to the family of natural planar Lyapunov orbits in the L_5 region. For the trajectory of the primary spacecraft, we compute the stable manifold of an assumed halo orbit and take a trajectory along the manifold that passes by Earth at an altitude of 200 km.

For the genetic algorithm, the vector of decision variables can be expressed as

$$\mathbf{x} = [\tau_p \quad \alpha_0 \quad \delta_0 \quad d_f \quad \tau_f \quad \alpha_f \quad \delta_f], \tag{67}$$

where τ_p determines the departing conditions along the primary spacecraft trajectory; more specifically, if T_p is the transfer time for the primary spacecraft along the stable manifold, the solar sail is deployed at $\tau_p T_p$. The variables α_0 and δ_0 are the cone and clock angle for the segment departing from the stable manifold of the periodic orbit which is again propagated for five years. The remaining variables are analogous to the ones described in §4.1.1 and §4.1.2.

For the multiple shooting differential corrector, the constraint $\mathring{G}$ in Eq. 60 can be used as the constraint on the initial node. However, the point $\boldsymbol{x}_0$ that defined the fixed periodic orbit now corresponds to the departure point at 200 km altitude of the primary spacecraft trajectory. Furthermore, The angles α and δ used with $\mathring{G}$ are the cone and clock angles for the selected halo orbit of the primary mission. For the constraint on the final node, both G (Eq. 11) and $\tilde{G}$ (Eq. 55) can be used; we choose the stronger periodicity constraint $\tilde{G}$. Therefore, the decision vectors for the initial and final nodes can be expressed

as:

$$\boldsymbol{X}_1 = \begin{bmatrix} \boldsymbol{x}_1 \\ \alpha_1 \\ \delta_1 \\ t_1 \\ \tau_p \end{bmatrix}, \quad \boldsymbol{X}_n = \begin{bmatrix} \boldsymbol{x}_n \\ T_n \\ \tilde{t}_n \end{bmatrix} \tag{68}$$

and the constraints are defined as:

$$g_0(\boldsymbol{X}_1) = \mathring{G}(\boldsymbol{x}_1, \tau_p) = \phi_{\tau_p}(\boldsymbol{x}_0, \alpha, \delta) - \boldsymbol{x}_1, \tag{69}$$

$$g_f(\boldsymbol{X}_n) = \tilde{G}(\boldsymbol{x}_n, T_n, \tilde{t}_n) = \phi_{T_n}(\phi_{\tilde{t}_n}(\boldsymbol{x}_n, \alpha, \delta), \alpha, \delta) - \phi_{\tilde{t}_n}(\boldsymbol{x}_n, \alpha, \delta). \tag{70}$$

5. Mission design results

This section describes the results obtained with the genetic algorithm in combination with the multiple shooting differential corrector and continuation for the cases considered.

5.1. Transfers between the collinear equilibrium points and families of periodic orbits in the L_5 region

We first apply the methodology described for transfers between the (displaced) collinear Lagrange points in the vicinity of Earth and natural and solar-sail families of planar Lyapunov orbits (PLOs) in the L_5 region. To check the quality of the solutions, we take the arrival orbits obtained with the differential corrector + continuation and we compute time-optimal transfers to such orbits using the optimal control solver PSOPT, which is a C++ implementation of the direct Legendre pseudospectral method [31]. As initial guess, we take the solution given by the differential corrector. Note that the problem solved with PSOPT is different from the problem solved with the differential corrector: the arrival conditions are no longer constrained to a family of periodic orbits but to a specific orbit. The TOF for the transfers obtained with the differential corrector + continuation (DC) and with PSOPT are given in Table 1 for $\beta \in \{0.01, 0.02, ..., 0.05\}$.

Table 1: TOF in days for transfers from the (displaced) L_1 and L_2 points to families of planar Lyapunov orbits in the L_5 region. The fastest cases for each lightness number departing from the (displaced) L_1 and L_2 points are given in bold.

Method	$\beta = 0.01$		$\beta = 0.02$		$\beta = 0.03$		$\beta = 0.04$		$\beta = 0.05$	
	DC	PSOPT	DC	PSOPT	DC	PSOPT	DC	PSOPT	DC	PSOPT
$L_1 \to$ natural PLOs	**943**	962	**612**	613	**486**	486	**434**	435	**402**	418
$L_1 \to$ solar-sail PLOs	1094	1061	729	727	575	574	512	513	478	524
$SL_1 \to$ natural PLOs	1094	1019	685	686	563	570	512	525	481	496
$SL_1 \to$ solar-sail PLOs	1194	1136	801	803	651	664	589	605	555	611
$L_2 \to$ natural PLOs	**846**	846	599	**598**	481	**480**	429	**428**	396	396
$L_2 \to$ solar-sail PLOs	941	940	712	711	571	570	508	508	474	477
$SL_2 \to$ natural PLOs	920	919	672	671	551	550	494	493	458	457
$SL_2 \to$ solar-sail PLOs	1015	1014	784	783	642	647	575	574	509	494

When comparing the results obtained with the differential corrector and with PSOPT, PSOPT sometimes converges to slightly different TOF values for transfers starting from the natural or displaced L_1 points. The differences are most noticeable for $\beta = 0.01$ due to the fact that the initial guesses include multi-revolution spirals around Earth, which introduces convergence difficulties for both methods. For $\beta = 0.05$ and departure from the L_1 and SL_1 points, the differences are also significant; however, in this case PSOPT converges to slower transfers. On the other hand, when the transfers depart from the natural or displaced L_2 points, both PSOPT and the differential corrector converge to practically the same solution. Generally, the optimised transfers with PSOPT are very close to the ones obtained with the differential corrector + continuation, indicating that PSOPT is not capable of further reducing the TOF beyond that obtained with the differential correction + continuation. Even though the differential corrector explores entire families of periodic orbits, the solution it produces is very close to the time-optimal solution for a transfer to a fixed arrival orbit. It is therefore concluded that the differential corrector in combination with the continuation method is an efficient tool to optimise the transfers. Consequently, from this point on, only the differential corrector will be used to produce time-optimal trajectories.

Figure 30 shows the fastest results for each case and lightness number from Table 1 in a bar plot. It is then clear how, for every lightness number, the fastest
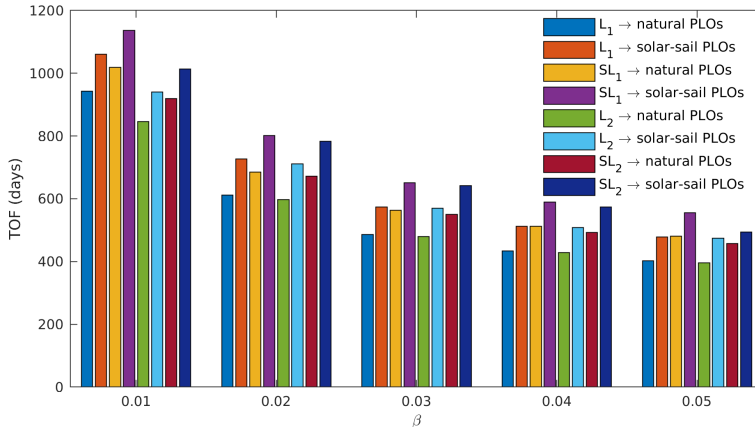
Figure 30: Fastest results from Table 1 in a bar plot.

transfers are obtained for departure from the L_1 and L_2 points and arriving at the family of natural planar Lyapunov orbits around the L_5 point. We include in Fig. 31 the fastest transfers and the control profiles for $\beta = 0.02$ (cases in bold in Table 1 for $\beta = 0.02$). The sail normal and the control profile show that, despite the constant stepwise control used for the differential corrector, the sail normal along the transfer and the control profiles are generally smooth. However, in the neighbourhood of Earth, the controls are more discontinuous, see top plot in Fig. 31. Note that in the zoomed plots, the Earth is represented as a blue dot and the sphere of influence of Earth is included as a blue dotted circle.

5.2. Transfers between families of periodic orbits

We apply the methodology described in §4.2.2 to compute transfers departing from the families of planar Lyapunov and halo orbits around the collinear equilibrium points in the vicinity of Earth and arriving at families of natural and solar-sail planar Lyapunov orbits in the L_5 region. It was seen that for some cases the differential corrector converged to trajectories with a large TOF. Therefore, we do a robustness analysis and compare the results with those obtained with the method described in §4.2.1 but applied to transfers between
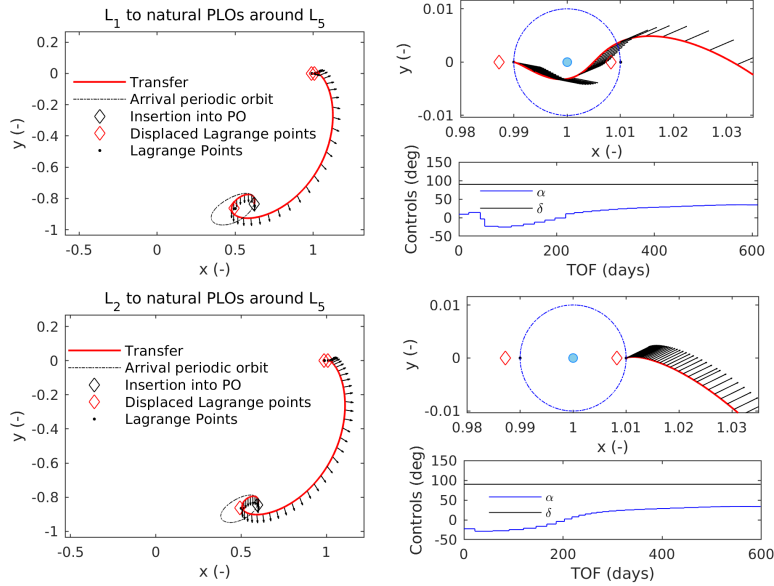
Figure 31: Transfers for $\beta = 0.02$ departing from L_1 (top) and from L_2 (bottom) to natural PLOs around L_5. Close-ups in the vicinity of Earth and the controls are included on the right.

periodic orbits. We refer to the approach followed in §4.2.2, as method DC1. For the second method, referred to as DC2, the genetic algorithm explores the departure families of periodic orbits and defines the departure conditions which are then kept fixed. Table 2 shows the results obtained for transfers departing from families of planar Lyapunov orbits and Table 3 for transfers departing from families of halo orbits (HO).

The results show that for almost all cases contained in Tables 2 and 3, the DC2 method converges to faster transfers. However, in some cases the DC1 produces better results, showing a reduction in the TOF by over 100 days with respect to the transfers obtained with the DC2 method. One such example is for the solar-sail PLOs around $SL_1 \rightarrow$ natural PLOs case for $\beta = 0.01$, where the gain is of 115 days. Since the departure periodic orbits are unstable, it seems that when the initial conditions are allowed to vary, the differential corrector is less robust than the version described in §4.2.1.

51

Table 2: TOF in days for transfers between families of planar Lyapunov orbits around the (displaced) L_1 and L_2 points and families of planar Lyapunov orbits in the L_5 region. The fastest cases for each lightness number departing from the families around the (displaced) L_1 and L_2 points are given in bold.

	$\beta = 0.01$		$\beta = 0.02$		$\beta = 0.03$		$\beta = 0.04$		$\beta = 0.05$	
Method	DC1	DC2	DC1	DC2	DC1	DC2	DC1	DC2	DC1	DC2
Natural PLOs around L_1 → natural PLOs	901	**858**	622	**609**	492	**490**	431	**430**	404	**400**
Natural PLOs around L_1 → solar-sail PLOs	978	957	732	725	584	572	526	509	485	478
Solar-sail PLOs around SL_1 → natural PLOs	870	985	1175	688	497	567	473	513	401	479
Solar-sail PLOs around SL_1 → solar-sail PLOs	1061	1036	1053	805	1409	657	533	589	793	555
Natural PLOs around L_2 → natural PLOs	**813**	818	611	**574**	488	**467**	447	**420**	405	**392**
Natural PLOs around L_2 → solar-sail PLOs	913	907	718	692	573	550	519	497	491	472
Solar-sail PLOs around SL_2 → natural PLOs	923	921	696	689	568	553	500	488	463	454
Solar-sail PLOs around SL_2 → solar-sail PLOs	1048	1002	791	761	658	624	599	579	537	518

Table 3: TOF in days for transfers between families of halo orbits around the (displaced) L_1 and L_2 points and families of planar Lyapunov orbits in the L_5 region. The fastest cases for each lightness number departing from the families around the (displaced) L_1 and L_2 points are given in bold.

	$\beta = 0.01$		$\beta = 0.02$		$\beta = 0.03$		$\beta = 0.04$		$\beta = 0.05$	
Method	DC1	DC2	DC1	DC2	DC1	DC2	DC1	DC2	DC1	DC2
Natural HOs around L_1 → natural PLOs	927	**874**	630	**607**	523	**493**	476	**433**	428	**404**
Natural HOs around L_1 → solar-sail PLOs	1190	962	744	733	601	573	524	516	510	483
Solar-sail HOs around SL_1 → natural PLOs	1111	972	865	703	702	558	436	519	461	476
Solar-sail HOs around SL_1 → solar-sail PLOs	1203	1086	930	810	805	671	497	594	549	554
Natural HOs around L_2 → natural PLOs	852	**827**	600	**583**	481	**468**	440	**420**	419	**391**
Natural HOs around L_2 → solar-sail PLOs	952	920	715	701	581	556	509	498	480	474
Solar-sail HOs around SL_2 → natural PLOs	934	925	706	698	553	553	560	486	470	453
Solar-sail HOs around SL_2 → solar-sail PLOs	1059	1033	820	778	651	648	586	543	545	529

Let us define the sets of invariant objects $\mathcal{I}_p^\beta$ as the sets of invariant objects with lightness number β associated with the equilibrium point p. So, for example, $\mathcal{I}_{L_1}^0$ contains the L_1 point, the families of planar and vertical Lyapunov and halo orbits around L_1, their invariant manifolds and the families of invariant tori associated with these families of periodic orbits. On the other hand, the set $I_{L_5}^0$ contains the L_5 point, the families of planar and vertical Lyapunov orbits around L_5 and the families of invariant tori associated with these families of periodic orbits. We can then express the transfers using the sets of departure invariant objects $\mathcal{D}_p^\beta$ and the sets of arrival invariant objects $\mathcal{A}_p^\beta$. So far, we have only explored transfers departing from subsets of D_p^β and arriving to subsets of $\mathcal{A}_p^\beta$. For the departure conditions, we explored the subsets $\tilde{\mathcal{D}}_p^\beta \subset \mathcal{D}_p^\beta$

with $p \in \{L_1, SL_1, L_2, SL_2\}$, which contain the equilibrium point p, families of planar Lypaunov and families of halo orbits associated with p. The arrival conditions explored are elements of the subsets $\tilde{\mathcal{A}}_p^\beta \subset \mathcal{A}_p^\beta$ with $p \in \{L_5, SL_5\}$, which contain the family of planar Lyapunov orbits associated with p. Tables 2 and 3 show that it is always faster to travel between families of natural periodic orbits. Furthermore, when comparing the TOFs in Tables 2 and 3 with those in Table 1, the results show that, with the exception of $\tilde{\mathcal{D}}_{L_1, SL_1}^{0.01}$, the time of flight for the transfers from elements of $\tilde{\mathcal{D}}_{p_1}^\beta$, with $p_1 \in \{L_1, SL_1, L_2, SL_2\}$, to elements of $\tilde{\mathcal{A}}_{p_2}^\beta$, with $p_2 \in \{L_5, SL_5\}$, does not vary much with the elements of $\tilde{\mathcal{D}}_{p_1}^\beta$ but it does with p_1 and p_2, i.e., the time of flight of the transfers is mainly affected by the equilibrium point the departure and arrival invariant objects are associated with. When the departure conditions are elements of $\tilde{\mathcal{D}}_{L_1, SL_1}^{0.01}$, departing from a family of periodic orbits was faster than departing from the L_1 or SL_1 points as for such trajectories, no revolutions around Earth are needed to reach the L_5 region. For a better visualisation of the results from Tables 2 and 3, we plot in Fig. 32 the time of flight of the transfers as a function of the lightness number for the cases departing from the invariant objects associated with the L_1 (top) and the L_2 (bottom) points and arriving to natural (left) and solar-sail (right) planar Lyapunov families in the L_5 region. It is clear how, for departure from the L_1 point and $\beta = 0.01$, departing from a family of periodic orbits is faster, whereas for $\beta > 0.01$ or departure from objects associated with the L_2 point, it does not make much of a difference. Instead, the arrival conditions have a much larger effect on the time of flight, as it can be seen that, for all departure conditions represented, arriving at solar-sail planar Lyapunov orbits in the L_5 region is considerably slower than arriving at their natural counterparts.

In order to visualise the transfers from the families of planar Lyapunov and halo orbits, we show in Figs. 33 and 34 the two fastest cases, including the control profile, for $\beta = 0.02$ (cases in bold in Tables 2 and 3 for $\beta = 0.02$). The transfers are very similar to those departing from the collinear equilibrium points. Again, the sail normal along the transfers and the control profile are generally smooth with the exception of when the departing conditions are in
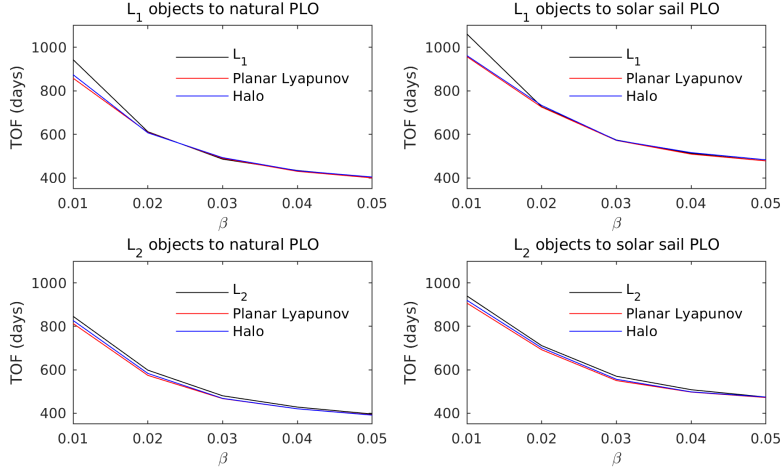
Figure 32: Time of flight as a function of the lightness number for transfers departing from objects associated with the L_1 (top) and L_2 (bottom) points and arriving to the families of natural (left) and solar-sail (right) planar Lyapunov orbits in the L_5 region.

the vicinity of the L_1 point and the spacecraft flies by Earth. Note that for the transfers departing from halo orbits $\delta \neq \pi/2$.

5.3. Transfers between families of quasi-periodic orbits

We now explore whether a gain in terms of TOF can be obtained when the departure and arrival invariant objects are families of quasi-periodic orbits. Therefore, we explore transfers between families of quasi-periodic orbits with the same Jacobi constant as the orbits that the differential corrector converged to in the previous section. Note that we only intend to determine whether transfers between families of quasi-periodic orbits are faster than the results obtained in §5.1 and §5.2 as opposed to providing the whole picture; therefore, we restrict the study to transfers between *natural* Lissajous families around the L_1 point to *natural* families of quasi-periodic orbits around the L_5 point for $\beta \in \{0.01, 0.02, ..., 0.05\}$. For the arrival conditions, we consider both the planar and out-of-plane families of quasi-periodic orbits (QPO) that exist around the planar Lyapunov orbits around the L_5 point. The results are given in Table

54
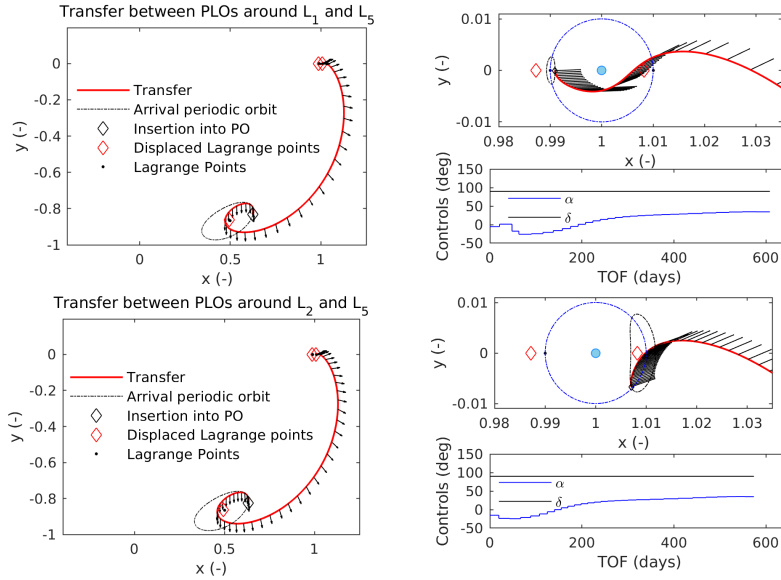
Figure 33: Transfers for $\beta = 0.02$ departing from natural PLOs around L_1 (top) and L_2 (bottom) to natural PLOs around L_5. Close-ups in the vicinity of Earth and the controls are included on the right.

4, where the TOF for the transfers between families of natural PLOs around L_1 and PLOs around L_5 is also included for comparison. The table shows that targeting a planar or an out-of-plane quasi-periodic orbit around L_5 results in similar TOF values. Furthermore, when comparing the TOF with those for transfers between periodic orbits, the switch to quasi-periodic orbits only results in a decrease in TOF of a few days. It might seem reasonable to expect the transfers to be faster when travelling between quasi-periodic orbits because of the increased freedom for the arrival conditions; however, this is not the case. So far the results have suggested that when the departure conditions are elements of $\tilde{D}_p^\beta$ with $\beta > 0.01$ and $p \in \{L_1, SL_1, L_2, SL_2\}$ the TOF does not change much with the elements of $\tilde{D}_p^\beta$ and is mainly affected by the arrival conditions. The number of degrees of freedom for the last node constrained to a family of periodic orbits and to a quasi-periodic orbit is the same: for a quasi-periodic orbit they are two, given by the 2-dimensional invariant torus, while for a family

55
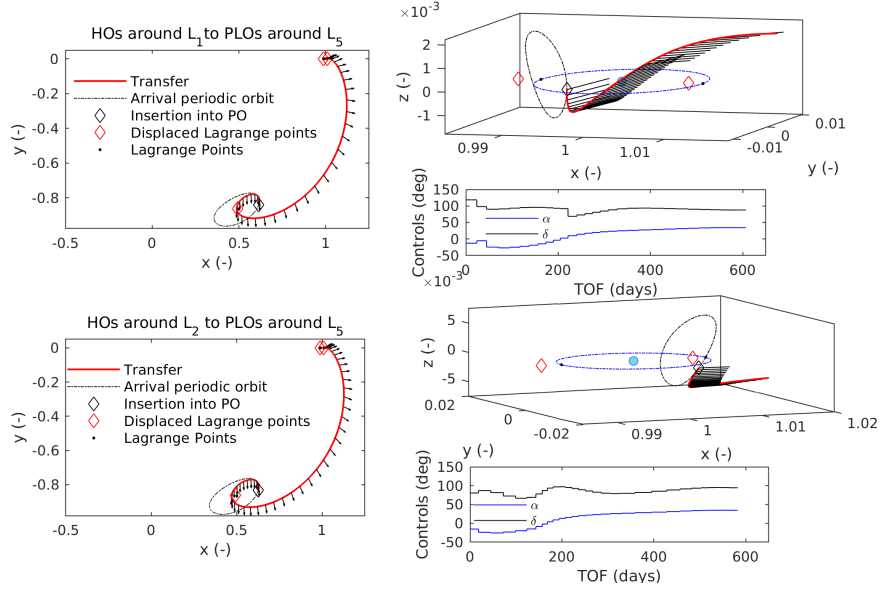
Figure 34: Transfers for $\beta = 0.02$ departing from natural HOs around L_1 (top) and L_2 (bottom) to natural PLOs around L_5. Close-ups in the vicinity of Earth and the controls are included on the right.

of periodic orbits, one degree of freedom is given by the 1-dimensional periodic orbit and another one by the family. The fact that for all scenarios the arrival conditions have two degrees of freedom might explain why the TOF does not change much when travelling to a quasi-periodic instead of a family of periodic orbits.

Table 4: TOF in days for transfers between families of natural Lissajous orbits around vertical Lyapunov orbits around L_1 and families of natural planar and out-of-plane quasi-periodic orbits around PLOs around L_5. The TOF for transfers between families of natural PLOs around L_1 and families of natural PLOs around L_5 is also included.

	$\beta = 0.01$	$\beta = 0.02$	$\beta = 0.03$	$\beta = 0.04$	$\beta = 0.05$
Lissajous around $L_1 \rightarrow$ planar QPO	857	605	481	431	397
Lissajous around $L_1 \rightarrow$ out-of-plane QPO	859	609	484	435	402
Natural PLOs around $L_1 \rightarrow$ natural PLOs	858	609	490	430	400

As an example, Fig. 35 presents the transfer, controls and a close-up in the vicinity of Earth and the L_5 region for the transfer to a planar quasi-periodic

orbit for $\beta = 0.02$. The figure shows how, again, the control profile is generally smooth but with more prominent discontinuities when the spacecraft is close to Earth.
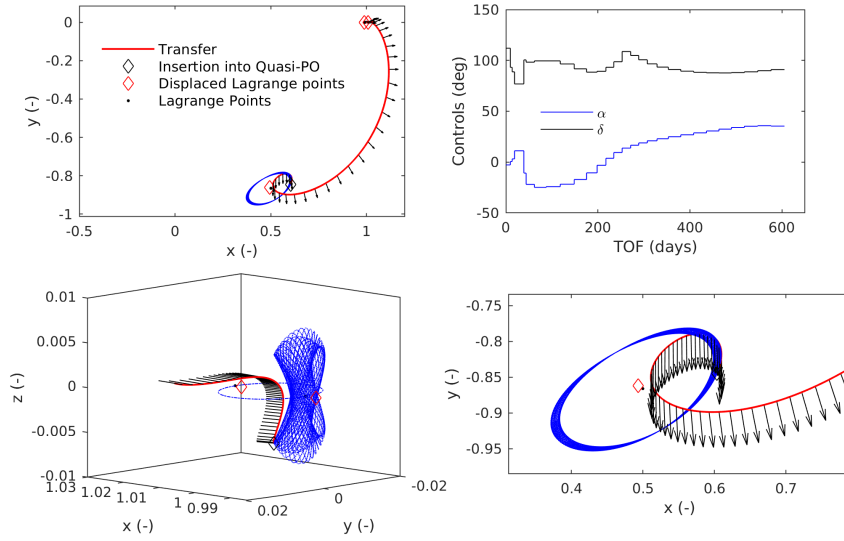
Figure 35: Transfer for $\beta = 0.02$ departing from a natural Lissajous orbit around L_1 (top left) and controls (top right). Close-ups in the vicinity of Earth (bottom left) and L_5 (bottom right) are also included.

5.4. Additional case

The last case considered is the case where the solar sail is launched as a secondary payload and the primary mission is travelling along the stable manifold of a natural halo orbit around the L_1 point. After separation from the primary spacecraft, the solar sail, with a sail performance of $\beta = 0.02$, starts its trajectory towards the family of natural planar Lyapunov orbits around the L_5 point. The assumed trajectory of the primary mission departs from Earth at a 200 km altitude and takes 206 days to reach its target halo orbit. The combination of the genetic algorithm and the differential corrector results in a solar-sail transfer with a TOF of 618 days. Note that the transfer takes longer

than when the solar sail departs from the family of natural halo orbits around L_1 for which a TOF of 607 days was obtained, see Table 3. This is not surprising, since for the case where the spacecraft departs from the family of halo orbits, the departure orbit was optimised to reduce the TOF. Nevertheless, the TOF is also very close to those where the departure conditions are elements of $\tilde{\mathcal{D}}_{L_1}^{0.02}$ and also for the case where the spacecraft travels between quasi-periodic orbits. Figure 36 depicts the transfer, the controls and close-ups in the vicinity of Earth and the L_5 point. The figure in the bottom left shows how, at some point along the primary spacecraft trajectory (depicted in blue) the solar sail starts its transfer to the L_5 region. Again, the sail normal and the control profile are generally smooth being more discontinuous in the vicinity of Earth.
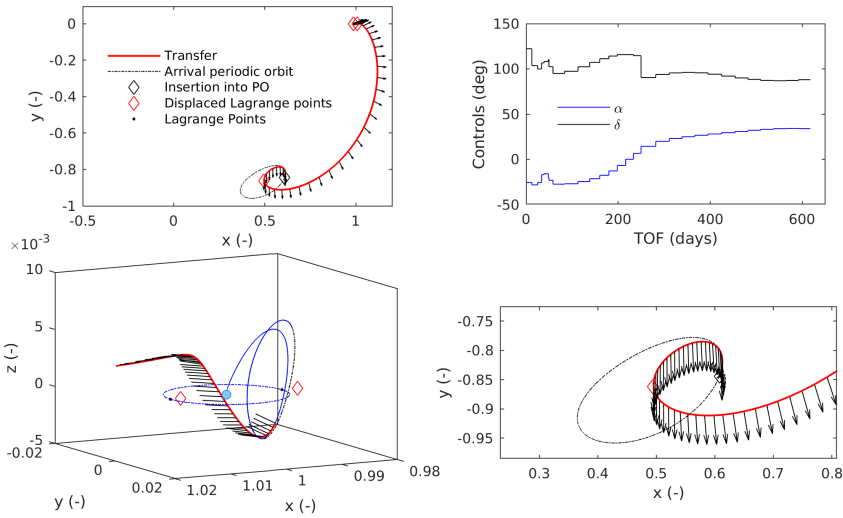
Figure 36: Transfer for $\beta = 0.02$ departing from the stable manifold of a natural halo orbit around L_1 (top left) and controls (top right). Close-ups in the vicinity of Earth (bottom left) and L_5 (bottom right) are also included.

58

6. Conclusions

This paper investigated solar-sail invariant objects in the vicinity of Earth and the L_5 region and transfers between them.

From geometric comparisons between families of planar Lyapunov orbits around the (displaced) L_2 point, vertical Lyapunov orbits around the (displaced) L_2 point and halo orbits around the (displaced) L_1 point it was concluded that a change in behaviour occurs for a lightness number $\beta^* \in (0.03, 0.04)$. This suggests that there is a qualitative change in the dynamics in the vicinity of Earth for β^*. No changes in the trends of the stability parameters were detected.

Families of solar-sail invariant tori were successfully computed by searching for invariant curves under a stroboscopic map. It was shown that quasi-periodic orbits exist also in the circular restricted three-body problem when solar radiation pressure is included around the elliptic, planar and vertical Lyapunov orbits as well as halo orbits. Furthermore, for Jacobi constant values smaller than that at the bifurcation of the planar Lyapunov family into the halo family, the families of quasi-periodic orbits around the vertical and planar Lyapunov orbits are connected.

For the mission design between invariant objects in the vicinity of Earth and the L_5 region, a novel methodology was proposed. Such approach allows to consider, as boundary conditions, equilibrium points, fixed periodic orbits, full families of periodic and quasi-periodic orbits and invariant manifolds, showing the versatility of the method. The proposed multiple shooting differential corrector in combination with a continuation method converged to feasible trajectories from the initial guesses that were generated with a genetic algorithm and allowed to reduce the time of flight (TOF) of the transfers. Furthermore, it was concluded that the method is a versatile tool capable of obtaining close to time-optimal transfers.

For the transfers between periodic orbits, a constraint was proposed which can, in itself, be used to compute periodic orbits. Such constraint improved the convergence of the differential corrector; however, with a few exceptions,

faster transfers were produced when the initial conditions were fixed instead of using the proposed constraint. Except for the cases with a lightness number of $\beta = 0.01$, the choice for the departure conditions, i.e., equilibrium points or invariant objects associated to them, does not significantly affect the time of flight. For $\beta = 0.01$, some revolutions around Earth are necessary to reach the L_5 region from the L_1 and SL_1 points, which make these transfers slow. While the departure invariant object do not generally have a large effect on the time of flight, the equilibrium point these invariant object are associated with does matter. When arriving to the same invariant object, departing from objects associated to the natural L_1 or L_2 points is faster. For the arrival conditions, it was also concluded that the equilibrium point the invariant objects are associated with affect significantly the time of flight. In fact, targeting families of natural planar Lyapunov orbits (associated with L_5) was considerably faster than targeting their solar-sail counterparts (associated with SL_5).

The TOF for transfers between quasi-periodic orbits were only a few days faster than for the other cases considered.

Fast solar-sail transfers taking between 391 and 1194 days, depending on the sail performance and the case, were shown to be feasible, where the fastest transfers were always between natural invariant objects.

References

[1] Gopalswamy, N., Davila, J. M., Cyr, O. C. St., Sittler, E. C., Auchère, F., Duvall, Jr. T. L., Hoeksema, J. T., Maksimovic, M., MacDowall, R. J., Szabo, A. and Collier, M. R., Earth-Affecting Solar Causes Observatory (EASCO): A potential International Living with a Star Mission from Sun-Earth L_5, Journal of Atmospheric and Solar-Terrestrial Physics 73 (5-6) (2011) 658–663.

[2] John, K. K., Graham, L. D. and Abell, P. A., Investigating Trojan Asteroids at the L_4/L_5 Sun-Earth Lagrange Points, in: Lunar and Planetary Science Conference, The Woodlands, Texas, USA, 2015.

[3] Llanos, P. J., Miller, J. K. and Hintz, G. R., L_5 Mission Design Targeting Strategy, in: AAS/AIAA Astrodynamicist Specialist Conference, Kauai, Hawaii, USA, 2013.

[4] Lo, M. W., Llanos, P. J. and Hintz, G. R., An L_5 Mission to Observe the Sun and Space Weather, Part I, in: AAS/AIAA Astrodynamicist Specialist Conference, San Diego, California, USA, 2010.

[5] McInnes, C. R., Solar Sailing - Technology, Dynamics and Mission Applications, Springer, 2017.

[6] Sood, R. and Howell, K., L_4, L_5 Solar Sail Transfers and Trajectory Design: Solar Observations and Potential Earth Trojan Exploration, in: 26th AAS/AIAA Space Flight Mechanics Meeting, Napa, California, USA, 2016.

[7] Farrés, A., Heiligers, J. and Miguel, N., Road Map to L_4/L_5 with a solar sail, in: AIAA 2018-0211 Space Flight Mechanics Meeting, Kissimmee, Florida, USA, 2018.

[8] Campbell, B. A. and Thomas, S. J., Realistic Solar Sail Thrust, in: Advances in Solar Sailing, Springer, 2014, pp. 407–435.

[9] Rios-Reyes, L. and Scheeres, D. J., Generalized Model for Solar Sails, Journal of Spacecraft and Rockets 42 (1) (2005) 182–185.

[10] Heiligers, J., Fernandez, J. M., Stohlman, O. R. and Wilkie, W. K., Trajectory Design for a Solar-Sail Mission to Asteroid 2016 HO3, in: AAS/AIAA Astrodynamics Specialist Conference. Snowbird, Utah, USA, 2018.

[11] Farrés, A., Transfer Orbits to L_4 with a Solar Sail in the Earth-Sun System, Acta Astronautica 137 (2017) 78–90.

[12] Perko, L., Differential Equations and Dynamical Systems, Vol. 7, Springer Science & Business Media, 2013.

[13] Breakwell, J. V. and Brown, J. V., The Halo Family of 3-Dimensional Periodic Orbits in the Earth-Moon Restricted 3-Body Problem, Celestial Mechanics 20 (4) (1979) 389–404.

[14] Howell, K. C., Three-Dimensional, Periodic, Halo orbits, Celestial Mechanics 32 (1) (1984) 53–71.

[15] Heiligers, J., Macdonald, M. and Parker, J. S., Extension of Earth-Moon Libration Point Orbits with Solar Sail Propulsion, Astrophysics and Space Science 361 (7) (2016) 241.

[16] Waters, T. J. and McInnes, C. R., Periodic Orbits Above the Ecliptic in the Solar-Sail Restricted Three-Body Problem, Journal of Guidance, Control, and Dynamics 30 (3) (2007) 687–693.

[17] Szebehely, V., Theory of Orbit: The Restricted Problem of three Bodies, Elsevier, 2012.

[18] Keller, H. B., Lectures on Numerical Methods in Bifurcation Problems, Applied Mathematics, 1987.

[19] Arnold, V. I., Kozlov, V. V. and Neishtadt, A. I., Mathematical Aspects of Classical and Celestial Mechanics, Vol. 3, Springer Science & Business Media, 2007.

[20] Farrés, A., Contribution to the Dynamics of a Solar Sail in the Earth-Sun System, Doctorial thesis, Universitat de Barcelona, 2009.

[21] Doedel, E. J., Romanov, A. V., Paffenroth, R. C., Keller, H. B., Dichmann, D. J., Galán-Vioque, J. and Vanderbauwhede, A., Elemental Periodic Orbits Associated with the Libration Points in the Circular Restricted 3-Body Problem, International Journal of Bifurcation and Chaos 17 (08) (2007) 2625–2677.

[22] Verrier, P., Waters, T. and Sieber, J., Evolution of the $\mathcal{L}_1$ Halo Family in the Radial Solar Sail Circular Restricted Three-Body Problem, Celestial Mechanics and Dynamical Astronomy 120 (4) (2014) 373–400.

[23] McInnes, A., Strategies for Solar Sail Mission Design in the Circular Restricted Three-Body Problem, MSE Thesis, School of Aeronautics and Astronautics, Purdue University, 2000.

[24] V. I. Arnold, Mathematical Methods of Classical Mechanics, Springer Science & Business Media, 2013.

[25] Jorba, A., A Methodology for the Numerical Computation of Normal Forms, Centre Manifolds and First Integrals of Hamiltonian Systems, Experimental Mathematics 8 (2) (1999) 155–195.

[26] Gómez, G. and Mondelo, J. M, The Dynamics Around the Collinear Equilibrium Points of the RTBP, Physica D: Nonlinear Phenomena 157 (4) (2001) 283–321.

[27] Olikara, Z. P and Scheeres, D. J., Numerical Method for Computing Quasi-Periodic Orbits and their Stability in the Restricted Three-Body Problem, Advances in the Astronautical Sciences 145 (2012) 911–930.

[28] Baresi, N., Olikara, Z. P. and Scheeres, D. J., Fully Numerical Methods for Continuing Families of Quasi-Periodic Invariant Tori in Astrodynamics, The Journal of the Astronautical Sciences 65 (2) (2018) 157–182.

[29] Farrés, A. and Jorba, À., Periodic and Quasi-Periodic Motions of a Solar Sail Close to SL_1 in the Earth-Sun System, Celestial Mechanics and Dynamical Astronomy 107 (1-2) (2010) 233–253.

[30] Koon, W. S., Lo, M. W. and Marsden, J. E. and Ross, S. D., Dynamical Systems, the Three-Body Problem and Space Mission Design, Citeseer, 2008.

[31] Becerra, V. M., Solving complex optimal control problems at no cost with PSOPT, in: Computer-Aided Control System Design (CACSD), 2010 IEEE International Symposium on, IEEE, 2010, pp. 1391–1396.

3

CONCLUSIONS AND RECOMMENDATIONS

3.1. CONCLUSIONS

This thesis aimed to improve the understanding of solar-sail bounded motion in the circular restricted three-body problem (CR3BP) by studying the different invariant objects in the system when solar radiation pressure (SRP) is included and determining what transfers are possible between invariant objects in the vicinity of Earth and the L_5 region with a versatile approach. A set of research questions was formulated in §1.4 that can be answered now and allow the research objectives to be fulfilled.

I. What kind of invariant objects exist in the CR3BP + SRP and what are their properties regarding existence, shape and stability?

Surfaces of equilibria, families of periodic and quasi-periodic orbits and their invariant manifolds exist when SRP is included in the CR3BP. The surfaces of equilibria contain the five Lagrange points and can merge for some range of the lightness number β. The equilibrium points in the ecliptic plane close to the L_1 and the L_2 points are unstable because of a saddle, whereas such points are surrounded by unstable equilibrium points due to a complex saddle. Regions of stable and almost stable equilibrium points exist, containing the triangular Lagrange points, and reach the neighbourhood of Earth. Lastly, a large region containing the L_3 point contains unstable equilibrium points also due to a saddle.

Families of natural and solar-sail planar and vertical Lyapunov orbits as well as families of halo orbits around the collinear equilibrium points in the vicinity of Earth exist. Additionally, families of planar and vertical Lyapunov orbits also exist around the natural and displaced L_5 points. The geometric behaviour of the families changes with the lightness number for the planar Lyapunov family around the displaced L_2 (SL_2), the vertical Lyapunov family around SL_2 and the halo family around the displaced L_1 (SL_1). Regarding stability, the planar and vertical Lyapunov families in the vicinity of Earth are unstable. For the halo families, ranges of stable and unstable orbits exist. Lastly, the planar and vertical Lyapunov families in the L_5 region are always stable.

For all the natural and solar-sail families considered, there exist orbits with a central part and therefore, such orbits are surrounded by families of quasi-periodic orbits. The families of invariant tori around planar and vertical Lyapunov orbits in the vicinity of Earth for values of the Jacobi constant smaller than that at the bifurcation of the planar Lyapunov family into the halo family, are connected, i.e., they are essentially the same family. For larger values of the Jacobi constant, close to those at the bifurcation point, quasi-periodic motion around planar Lyapunov orbits does not exist but it does around vertical Lyapunov and halo orbits. For even larger values of the Jacobi constant, the planar Lyapunov orbits regain their central part and quasi-periodic motion exists around the planar and vertical Lyapunov and halo orbits. Regarding invariant tori in the L_5 region, the planar and vertical Lyapunov orbits are always surrounded by families of quasi-periodic orbits. Two different types of families of quasi-periodic orbits were found around the planar Lyapunov orbits, whereas one type was found around the vertical Lyapunov orbits. A matrix that is a by-product for the computation of quasi-periodic orbits contains stability information of the quasi-periodic orbits. The quasi-periodic orbits in the vicinity of Earth have stable and unstable manifolds which can be used in the mission design. However, a detailed study on the stability of the quasi-periodic orbits was beyond the scope of the thesis and it is left for future work.

The equilibrium points, periodic and quasi-periodic orbits in the vicinity of Earth have associated invariant manifolds which can be used to escape or be captured by these invariant objects. The objects in the L_5 region are stable and therefore do not have associated stable or unstable invariant manifolds.

II. What is the effect of the lightness number on the properties of the invariant objects found under I.?

Regarding the surfaces of equilibria, for $\beta \in \{0.01, 0.02\}$, there exist three surfaces: one containing L_1, one containing L_2 and a last one containing the L_3, L_4 and L_5 points. For larger lightness numbers, the surface containing L_3 and the triangular Lagrange points merges with the surface containing L_1. The general trends of the stability of the equilibrium points does not seem to change much with the lightness number; for the cases considered, the regions of unstable, almost stable and stable points are very similar.

Geometric comparisons for the families of periodic orbits showed that the orbits of the planar Lyapunov families around the SL_2 point start shifting their intersection with $\Lambda_2 = \{y = 0, \dot{y} < 0\}$ towards Earth for $\beta \in (0.03, 0.04)$. For a lightness number in the same range, the orbits of the vertical Lyapunov family around the SL_2 point get closer to the ecliptic plane until they collapse to planar orbits. Lastly, the orbits at the end of the halo family around SL_1 also collapse to the ecliptic plane instead of becoming near rectilinear halo orbits. The changes in the geometric behaviour of these families suggests a qualitative change in the dynamics, at least in the vicinity of Earth, for a lightness number $\beta^* \in (0.03, 0.04)$. Regarding the stability of the periodic orbits, the stability parameters presented some variation with the lightness number, but they generally preserved the same trends for all β.

The study of the effect of the lightness number on invariant tori is not straightforward. The families of invariant tori are 2-parameter families and they originate from each of the elliptic orbits of the families of periodic orbits. A study on the effect of the lightness number on quasi-periodic orbits would have to compare 2-parameter families of quasi-periodic orbits around different orbits at different β which was considered out of the scope of this thesis.

The invariant manifolds of the (displaced) L_1 and L_2 points can be used to escape from the vicinity of Earth and reach the L_5 region. However, trajectories along the unstable manifold of the L_1 point get entangled around Earth and do not reach the L_5 region. Manifold-like trajectories from L_1 that include a solar sail acceleration along the Sun-spacecraft line do successfully escape from Earth.

III. What approach is capable of computing time-optimal transfers between the invariant objects found under I.?

A multi-objective genetic algorithm in combination with a multiple shooting differential corrector and continuation proved to be an approach capable of computing near-time-optimal transfers considering a wide range of cases. Equilibrium points, fixed periodic orbits, families of periodic orbits, their invariant manifolds and families of quasi-periodic orbits could be considered as boundary conditions. Through a comparison with direct pseudospectral method, the transfers were shown to be close to time-optimal for the cases where the spacecraft departed from the collinear equilibrium points in the vicinity of Earth. Furthermore, the control profile for the transfers was quite smooth in spite of the constant step-wise control law adopted.

The approach is not restricted to the computation of transfers to the L_5 region; with only a few changes transfers reaching invariant objects in the L_4 region or even transfers between invariant objects associated with the collinear equilibrium points can be computed. Furthermore, the whole approach can be automatised.

IV. What are the departure and arrival invariant objects that result in the fastest transfers to the L_5 region?

The results showed that generally, the choice of departure conditions, i.e., departing from either of the collinear equilibrium points in the vicinity of Earth or the families of planar Lyapunov or halo orbits associated with the equilibrium points, did not have much of an effect on the time of flight of the transfers. What did have an effect on the time of flight was the equilibrium point associated with the departure and arrival invariant objects. Travelling between invariant objects associated with the L_2 and the L_5 points was fastest, followed by transfers between invariant objects associated with the L_1 and the L_5 points. Therefore, the results suggest that the fastest transfers between the vicinity of Earth and the L_5 region are those departing from and arriving to natural invariant objects. For $\beta = 0.01$, the transfers departing from the L_1 and SL_1 points took longer than the transfers departing from families of periodic

orbits associated with these points. For those cases, revolutions around Earth were necessary to reach the L_5 region, which were not required when the spacecraft departed from a family of periodic orbits.

It was also explored whether travelling between quasi-periodic orbits was faster than the previous cases. Transfers between natural Lissajous orbits around the vertical Lyapunov orbits around the L_1 point and natural planar and out-of-plane quasi-periodic orbits around planar Lyapunov orbits in the L_5 region were considered. The transfers had a very similar time of flight to those transfers departing from the L_1 point and the natural planar Lyapunov and halo families associated with L_1 and arriving to the family of natural planar Lyapunov orbits around L_5.

The answers to the research questions provide the necessary information to meet the research objectives to a great extent. Therefore, the goal of this thesis has been fulfilled.

3.2. RECOMMENDATIONS

in order to advance and further improve the contributions of this thesis, this section includes recommendations that were considered and thought of during the development of the scientific content but could not be implemented due to time constraints.

- Improve the computation of invariant tori at large values of the Jacobi constant.

  The method used for the computation of families of quasi-periodic orbits could successfully obtain the entire families at small values of the Jacobi constant. At large values, quasi-periodic orbits could still be computed, but the algorithm stopped converging before the entire families were computed. It is thought that the invariant curves need a larger number of harmonics when expressed in their Fourier series at larger energies. The method used implements a fixed number of points in the discretised curves and the same number of harmonics. Therefore, a method capable of increasing the number of harmonics or points of the invariant curves with the continuation of the families could work. In fact, a similar approach was implemented in Ref. [16]. The methodology used in this thesis was tested with a similar approach to vary the number of harmonics but there was no improvement. A multiple-shooting approach might also improve the method. Perhaps the implementation of both multiple shooting and variable harmonics number is necessary.

- Study the practical use of quasi-periodic orbits.

  Quasi-periodic orbits might provide better coverage of regions of the Sun or the Moon or be more stable than periodic orbits. Furthermore, quasi-periodic orbits might require less station-keeping for real missions. It is then worth to consider these objects and study for what practical use they might be better suited than periodic orbits.

- Study other constraints to target the families of unstable periodic orbits around the collinear equilibrium points.

  In order to constrain a node to a family of unstable periodic orbits, it was seen that a stronger periodicity constraint was necessary. A new constraint was proposed and the differential corrector improved. However, only for a few cases did it result in faster transfers than leaving the first node fixed, at least for the step size considered for the continuation. At smaller step sizes, it might improve at the cost of increasing the computational time. Studying other constraints to set a node to a family of unstable periodic orbits might allow faster transfers.

- Set inequality constraints on the multiple shooting differential corrector.

  Equality constraints are easy to implement on the multiple shooting differential corrector. However, inequality constraints are more challenging. Implementing inequality constraints in an efficient manner might allow the differential corrector to converge to faster transfers and consider more cases. For instance, inequality constraints for the controls, or the size of the departure or arrival orbits could be of interest.

- Improve the continuation of the solutions with the multiple shooting differential corrector.

  In this thesis, the solutions are continued using as initial guess the previous solution but reducing the imposed time of flight. This type of continuation is referred to as natural parameter continuation and it is one of the simplest methods. Using an improved predictor corrector method could improve the

differential corrector. Studying the kernel of the system or implementing a pseudo-arclength method could be a place to start.

- Target families of quasi-periodic orbits in the multiple shooting differential corrector.

  In this thesis, the departure and arrival quasi-periodic orbits for the optimisation with the multiple shooting differential corrector were fixed. Implementing the computation of invariant tori with the optimisation of the trajectory would allow to set the outer nodes to families of quasi-periodic orbits and the transfers could perhaps be further optimised.

- Use a higher fidelity model.

  The CR3BP in combination with the solar radiation pressure can be used for the preliminary design of space missions. However, for a more advanced stage in the mission design, it would be necessary to improve the dynamics including third-body perturbations and also use a more realistic sail model.

A

APPENDIX

A.1. VERIFICATION

In order to guarantee that the model and methods used and developed in this thesis are implemented correctly, a section on verification is included.

A.1.1. DYNAMICAL SYSTEM MODEL

The dynamical system can be modelled with a system of first order differential equations as

$$\dot{\boldsymbol{x}} = f(\boldsymbol{x}) \tag{A.1}$$

In order to verify such model, the intersection of the surfaces of equilibria with the ecliptic plane for $\beta \in \{0.01, 0.02, ..., 0.05\}$ are computed and checked with the results from Ref. [1]. Furthermore, using the convention from Ref. [1], sections of the surfaces of equilibria according to their stability are represented. Figure A.1 includes the results, whereas Fig. A.2 shows the sections obtained in Ref. [1]. Note that in Fig. A.1 the x-axis is reversed as in Ref. [1] the x-axis is the -x-axis used in the thesis. Since they are in good agreement with the literature, the dynamical model including the solar-sail acceleration is verified.
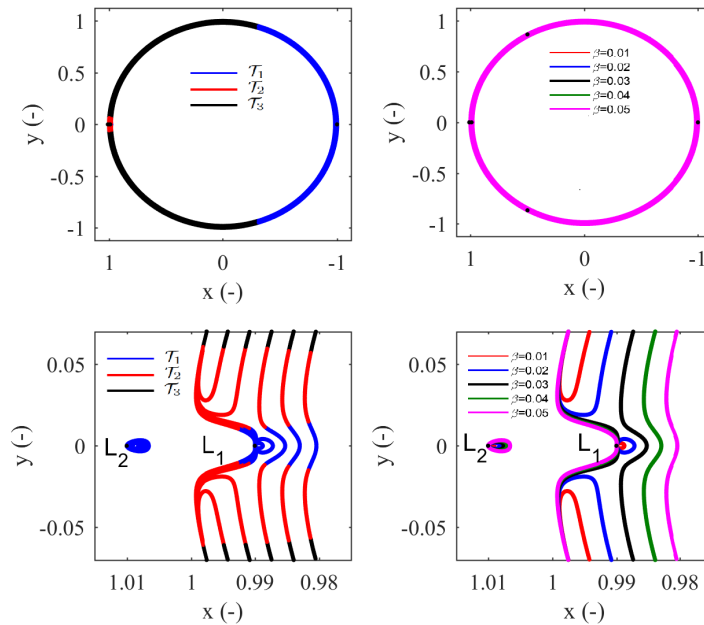
Figure A.1: Sections of the surfaces of equilibria with the ecliptic plane and their stability classification for $\beta \in \{0.01, 0.02, ..., 0.05\}$ (top) and close up in the neighbourhood of Earth (bottom).

75
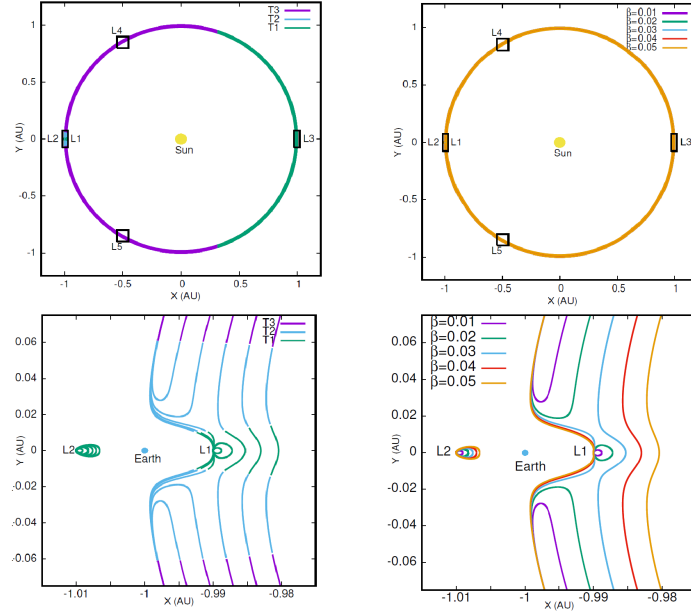
Figure A.2: Sections of the surfaces of equilibria with the ecliptic plane and their stability classification for $\beta \in \{0.01, 0.02, ..., 0.05\}$ (top) and close up in the neighbourhood of Earth (bottom) from Ref. [1].

A.1.2. PERIODIC ORBIT GENERATION

To verify the generation of periodic orbits is implemented correctly, it is enough to check for a family of periodic orbits whether the orbits are closed. Therefore, we take the family of solar-sail planar Lyapunov orbits around the SL_1 point for $\beta = 0.02$ and compute the norm of the difference between the first and the last point of the orbit. Figure A.3 shows the error for each orbit of the family. Since the error is of the order of 10^{-9}, the generation of periodic orbits is verified.
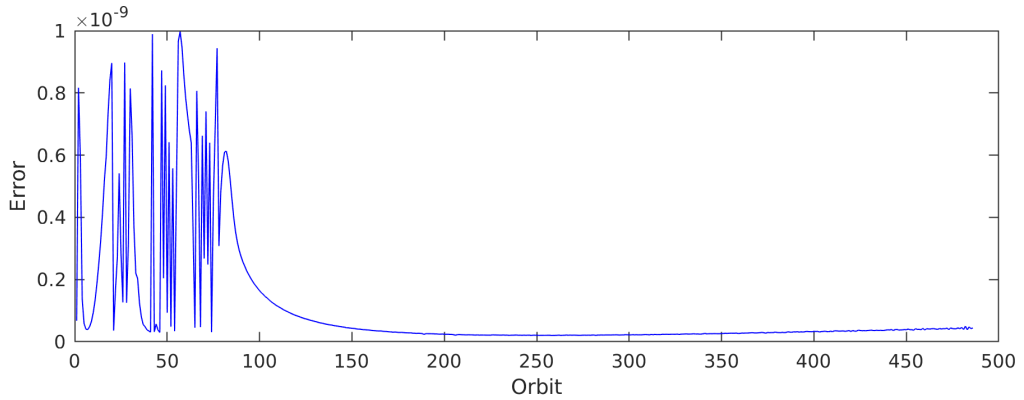
Figure A.3: Error for the solar-sail planar Lyapunov orbits around the SL_1 point for $\beta = 0.02$.

A.1.3. INVARIANT TORI GENERATION

To verify the computation of periodic orbits, we simply checked that the flow comes back to the same point after the period of the orbit. For quasi-periodic orbits, we can proceed in a similar way and check whether the flow comes back to the same curve. Note that this is in fact the property that is used for their computation. Therefore, we take a curve that is presumably invariant under the flow and compute the flow from each point of the curve for the period associated with the second frequency of the quasi-periodic orbit, i.e., the strobo-scopic time of the stroboscopic map. If the initial curve is indeed invariant under the flow, the image under the stroboscopic map needs to define the same curve. Therefore, we use spline interpolation for the invariant curve and the mapped curve, evaluate them at the same points and compute their difference. If they are the

same curve, then their difference should be of the order of the tolerance used for their computation. We will verify the computation of quasi-periodic orbits using a quasi-halo orbit around the SL_1 point for $\beta = 0.02$ and Jacobi constant $J_c = -2.9603$.

The invariant curves were discretised in $N = 35$ points, so for the spline interpolation it is desirable to have a larger number of points. The discretised curves, both the invariant curve and its image under the stroboscopic map, define continuous curves through the Fourier coefficients that can be obtained from the discrete data. We can therefore use the series to obtain any number of points in those curves by means of trigonometric interpolation. In fact, any curve φ expressed in Fourier series by its complex coefficients, can be written as

$$\varphi(\xi) = \sum_{k \in K} \boldsymbol{c}_k e^{ik\xi}, \tag{A.2}$$

where K is an index set. Then, by expanding the index set with respect to that of the original discretised curve, the number of points of the curves can be increased. We extrapolate the 35 nodes to 500 and then use spline interpolation and compute the difference between both interpolated curves evaluated at the same 500 points. Note that the spline interpolation is necessary to compute the curves at the same points since, in their Fourier representations, they are not necessarily parameterised by the same parameter. Figure A.4 shows the interpolation of the invariant curve (left) and the error between the interpolated invariant curve and its image under the stroboscopic map at each of the 500 points of the curves. Since the error is of the order of 10^{-11}, it can be concluded that both the invariant curve and its image define the same curve. Consequently, the generation of quasi-periodic orbits is verified.
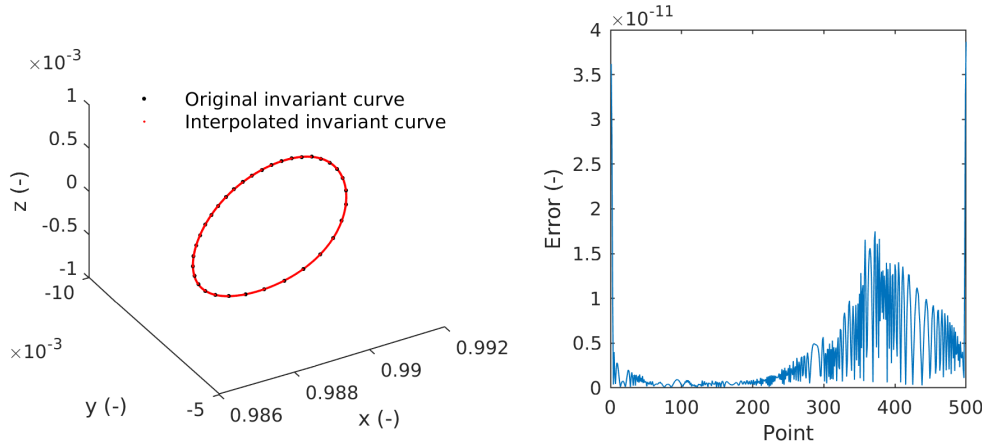
Figure A.4: Interpolated invariant curve (left) and error between the interpolated invariant and mapped curves (right).

A.1.4. INVARIANT MANIFOLDS GENERATION

The invariant manifolds associated with the equilibrium points are given by the eigenvectors of the linearisation of the dynamics at an equilibrium point, i.e., the Jacobian of f given in Eq. A.1. In order to verify the invariant manifolds associated with equilibrium points, it is sufficient to verify the Jacobian of f since the eigenvectors are computed with MATLAB® and are therefore assumed to be verified.

The dynamics were written in Mathematica® and then translated into MATLAB® code. Since the dynamics have already been verified, the dynamics written in Mathematica® and the translation function to MATLAB® code are also verified. The Jacobian of f was then computed with Mathematica® and since this is a reliable piece of software, the Jacobian of f is verified. Therefore, the invariant manifolds associated with equilibrium points are verified.

The invariant manifolds associated with periodic orbits are given by the eigenvectors of the monodromy matrix propagated along the orbit with the state transition matrix (STM). Note that the monodromy matrix is the STM evaluated after the period of the periodic orbit. Therefore, in order to verify the computation of the invariant manifolds of periodic orbits, it is sufficient to verify the STM or the monodromy matrix.

When the system is Hamiltonian, the monodromy matrix eigenvalues come in reciprocal pairs and two of them are unitary. We use the family of solar-sail planar Lyapunov orbits around the SL_1 point for $\beta = 0.02$ computed for the thesis and check whether the monodromy matrix satisfies the two unit eigenvalues and the reciprocity conditions. We compute the eigenvalues and select λ_a and λ_b that are the closest to 1. Then,

we plot $Real(\lambda_i) - 1$, $Imag(\lambda_i)$ and $|\lambda_i| - 1$, with $i = a, b$, for each orbit and check how close these eigenvalues are to one. Figure A.5 depicts the results. The figure shows that the real part has an error of the order of 10^{-9}, whereas the imaginary part has an error of the order of 10^{-5}. The norm of the unit eigenvalues has the smallest error and is of the order of 10^{-13}. Furthermore, both λ_a and λ_b have the same real part and the same magnitude, but with opposite imaginary part. Since the errors are quite small, it can be concluded that the monodromy matrix has two unit eigenvalues. To check the reciprocity condition, we simply com-
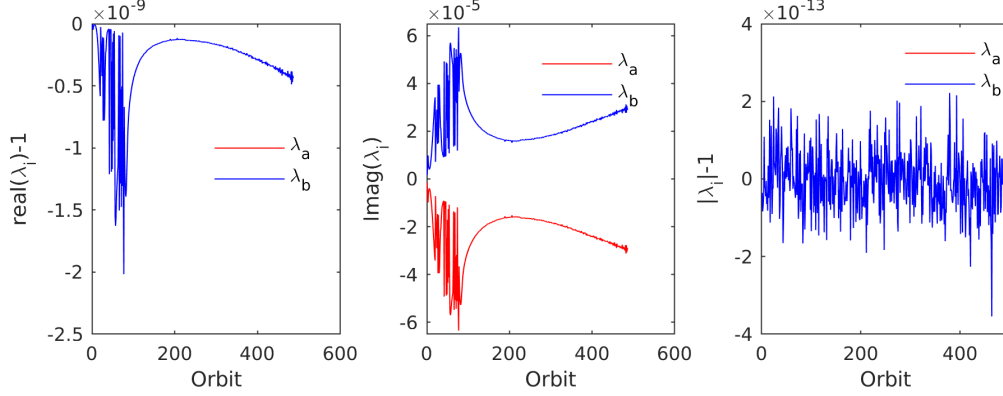
Figure A.5: Error in the unit eigenvalues of the monodromy matrix for the family of solar-sail planar Lyapunov orbits around the SL_1 point for $\beta = 0.02$.

pute the eigenvalues and compute $|\lambda_i - 1/\lambda_j|$ of those pairs $\{i, j\}$, with the exception of the unity ones, that seem reciprocal, i.e., pairs that satisfy $|\lambda_i - 1/\lambda_j| \approx 0$. Figure A.6 shows how for both pairs of eigenvalues, the reciprocity condition is met with an error in the order of 10^{-13} for the first pair and of the order of 10^{-14} for the second. Therefore, the mondromy matrix eigenvalues come in reciprocal pairs. Since the monodromy
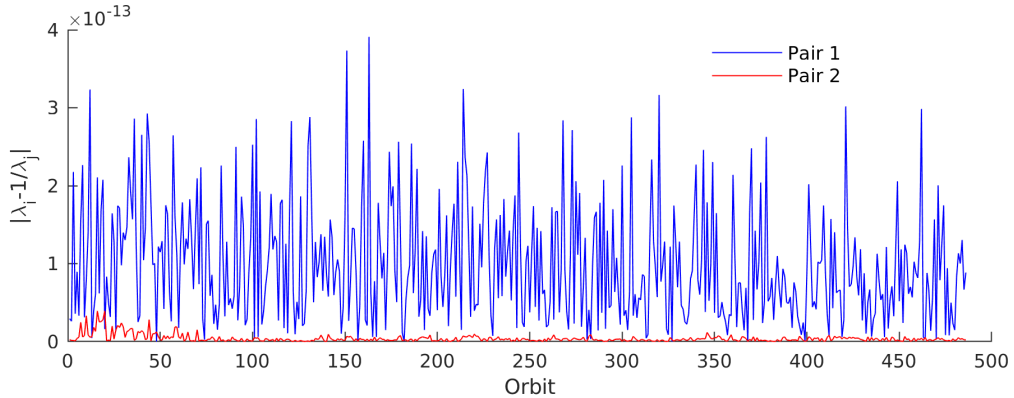
Figure A.6: Error on reciprocity of the eigenvalues of the monodromy matrix for the family of solar-sail planar Lyapunov orbits around the SL_1 point for $\beta = 0.02$.

matrix implemented has two unit eigenvalues and its eigenvalues come in reciprocal pairs, it is assumed to be verified, which verifies the invariant manifolds associated with periodic orbits.

For the invariant manifolds of quasi-periodic orbits, we followed Ref. [17] and obtained the stable and unstable directions required for the computation of the invariant manifolds from the eigenvectors of a stability matrix which is a by-product of the computation of quasi-periodic orbits. We assume the theory presented in Ref. [17] is validated; consequently, since the code for generating quasi-periodic orbits is verified, so is the computation of invariant manifolds of quasi-periodic orbits.

A.1.5. MULTIPLE SHOOTING DIFFERENTIAL CORRECTOR
In order to verify the multiple shooting differential corrector, we integrate the initial conditions of the solutions with the control profile obtained and check whether the constraints on the initial and final nodes are met for the scenarios considered.

For the case departing from the collinear equilibrium points and arriving at a family of periodic orbits in the L_5 region, we take the case where the solar sail departs from the L_1 point and arrives to the family of natural planar Lyapunov orbits around the L_5 point with $\beta = 0.02$. The norm of the difference between the first point of the transfer and the L_1 point is of the order of 10^{-13}. The last point of the transfer is integrated for the period of the periodic orbit it converged to and the norm of the difference between the first and last point was computed. The error in the constraint for the last node is of the order of 10^{-11}. Therefore, the multiple shooting differential corrector for the case where the solar sail departs from an equilibrium point and arrives at a family of periodic orbits in the L_5 region is verified.

For the multiple shooting differential corrector used for transfers between families of periodic orbits, i.e., implementing the stronger periodicity constraint, we check whether the outer nodes belong to periodic orbits for the case where the solar sail departs from the family of natural halo orbits around the L_2 point and it arrives to the family of natural planar Lyapunov orbits around the L_5 point for $\beta = 0.02$. The error on the first node is of the order of 10^{-12} and the error on the last node is of the order of 10^{-11}. Therefore, the multiple shooting differential corrector for transfers between families of periodic orbits that implements the stronger periodicity constraint is verified.

To verify the case where the outer nodes are constrained to quasi-periodic orbits, we will check whether the initial and final nodes belong to invariant curves of quasi-periodic orbits. We will do the check with the transfer between a natural Lissajous orbit around a vertical Lyapunov orbit around the L_1 point and a natural planar quasi-periodic orbit around a planar Lyapunov orbit around the L_5 point for $\beta = 0.02$. The constraint imposed on the outer nodes was that these nodes where equal to the flow from some point within an invariant curve $\varphi(\xi)$ after some time ζT_2, where T_2 is the period associated with the second frequency of the quasi-periodic orbit. Note that if $\varphi(\xi)$ is an invariant curve, $\phi_t(\varphi(\xi), \alpha, \delta)$ is also. Since the differential corrector finds a solution for ζ, we compute $\phi_{\zeta T_2}(\varphi(\xi), \alpha, \delta)$ and check whether the outer nodes belong to the curve. To perform that check, we proceed in a similar way as was done to verify the generation of quasi-periodic orbits. We use trigonometric interpolation with the Fourier series to obtain the curves $\phi_{\zeta T_2}(\varphi(\xi), \alpha, \delta))$ with 500 points. We then use a 6-dimensional spline to compute the point in the curve where the outer nodes are supposed to be and we compute the norm of the difference with the actual outer nodes. Figure A.7 depicts the original invariant curve, its image under $\phi_{\zeta T_2}$, the interpolated curve with the Fourier series, the periodic orbit and the initial point of the transfer. It is apparent that the node does belong to the propagated curve and is therefore constrained to a quasi-periodic orbit. In fact, the error of the first node is of the order of 10^{-11}, whereas for the last node the error is of the order of 10^{-12}. Therefore, the multiple shooting differential corrector for transfers between quasi-periodic orbits is verified.
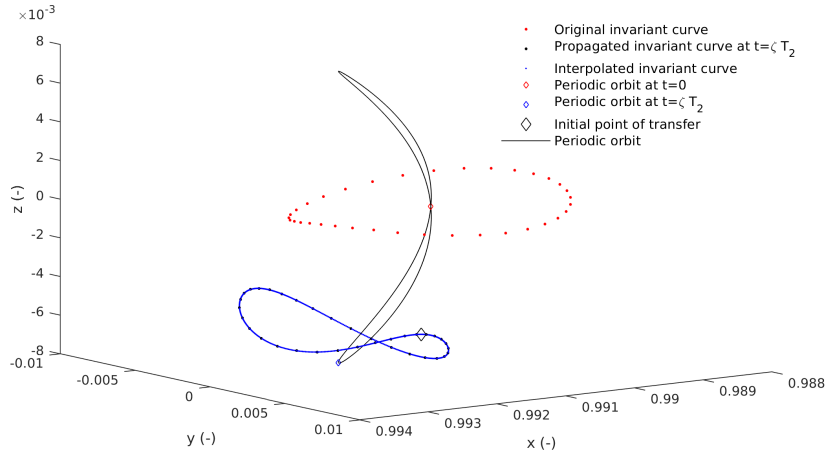
Figure A.7: Curves for the verification of the multiple shooting differential corrector for transfers between quasi-periodic orbits.

A.2. VALIDATION

In this section the dynamical system model is validated to guarantee the conclusions and results obtained are valid. Furthermore, the genetic algorithm is also validated to check that it does indeed obtain near-feasible initial guesses for the transfers.

A.2.1. DYNAMICAL SYSTEM MODEL

The dynamical system used in this study has been used in the literature extensively [1, 14, 15]. Therefore, it is assumed that the model is validated.

A.2.2. GENETIC ALGORITHM

The multi-objective genetic algorithm implemented for the computation of initial guesses presumably computes near-feasible trajectories for the cases considered that converge to feasible transfers with the multiple shooting differential corrector. The genetic algorithm is validated since the initial guesses that it produces do indeed converge as it was seen during the verification of the multiple shooting differential corrector.

REFERENCES

[1] Farrés, A., *Transfer Orbits to L_4 with a Solar Sail in the Earth-Sun System,* Acta Astronautica **137**, 78 (2017).

[2] McInnes, C. R., *Solar Sailing - Technology, Dynamics and Mission Applications* (Springer, 2017).

[3] Tsuda, Y., Mori, O., Funase, R., Sawada, H., Yamamoto, T., Saiki, T., Endo, T. and Kawaguchi, J., *Flight Status of IKAROS Deep Space Solar Sail Demonstrator,* Acta Astronautica **69**, 833 (2011).

[4] Alhorn, D. C., Casas, J. P., Agasid, E. F., Adams, C. L., Laue, G., Kitts, C. and O'Brien, S., *Nanosail-d: The Small Satellite that Could!* (2011).

[5] Ridenoure, R. W., Spencer, D. A., Stetson, D. A., Betts, B., Munakata, R., Wong, S. D., Diaz, A., Plante, B., Foley, J. D. and Bellardo, J. M., *Status of the Dual CubeSat LightSail Program,* in *AIAA SPACE 2015 Conference and Exposition*, p. 4424.

[6] McNutt, L., Johnson, L., Clardy, D., Castillo-Rogez, J., Frick, A. and Jones, L., *Near-Earth Asteroid Scout,* (2014).

[7] Lo, M. W., Llanos, P. J. and Hintz, G. R., *An L_5 Mission to Observe the Sun and Space Weather, Part I,* in *AAS/AIAA Astrodynamicist Specialist Conference, San Diego*, Vol. 136, pp. 10–121.

[8] Gopalswamy, N., Davila, J. M., Cyr, O.C.St., Sittler, E.C., Auchère, F., Duvall, T.L., Hoeksema, J.T., Maksimovic, M., MacDowall, R.J. and Szabo, A., *Earth-Affecting Solar Causes Observatory (EASCO): a Potential International Living with a Star Mission from Sun–Earth L_5,* Journal of Atmospheric and Solar-Terrestrial Physics **73**, 658 (2011).

[9] Szebehely, V. , *Stability of the Points of Equilibrium in the Restricted Problem,* The Astronomical Journal **72**, 7 (1967).

[10] John, K. K., Graham, L. D., Abell, P. A., *Investigating Trojan Asteroids at the L_4/L_5 Sun-Earth Lagrange Points,* (2015).

[11] Heiligers, J., Diedrich, B., Derbes, W. and McInnes, C. R., *Sunjammer: Preliminary End-to-End Mission Design,* in *AIAA/AAS Astrodynamics Specialist Conference* (2014) p. 4127.

[12] Llanos, P. J., Miller, J. K. and Hintz, G. R., *L_5 Mission Design Targeting Strategy,* in *AAS/AIAA Astrodynamicist Specialist Conference, Kauai, Hawaii, USA* (2013).

[13] Sood, R. and Howell, K., *L_4, L_5 Solar Sail Transfers and Trajectory Design: Solar Observations and Potential Earth Trojan Exploration,* in *26th AAS/AIAA Space Flight Mechanics Meeting, Napa, California, USA* (2016).

[14] Farrés, A., Heiligers, J. and Miguel, N., *Road Map to L_4/L_5 with a solar sail,* in *AIAA 2018-0211 Space Flight Mechanics Meeting, Kissimmee, Florida, USA* (2018).

[15] Farrés, A., *Contribution to the Dynamics of a Solar Sail in the Earth-Sun System,* Doctorial thesis (2009).

[16] Gómez, G. and Mondelo, J. M, *The Dynamics Around the Collinear Equilibrium Points of the RTBP,* Physica D: Nonlinear Phenomena **157**, 283 (2001).

[17] Olikara, Z. P. and Scheeres, D. J., *Numerical Method for Computing Quasi-Periodic Orbits and their Stability in the Restricted Three-Body Problem,* Advances in the Astronautical Sciences **145**, 911 (2012).